ELSEVIER

Journal of Fluids and Structures 24 (2008) 628–650

JOURNAL OF FLUIDS AND STRUCTURES

www.elsevier.com/locate/jfs

Pressure field analysis on oscillating circular cylinder

A. Zasso*, M. Belloli, S. Giappino, S. Muggiasca

Dipartimento di Meccanica, Politecnico di Milano, Via La Masa 34, 20156 Milano, Italy

Received 11 October 2005; accepted 24 November 2007
Available online 4 March 2008

Abstract

The flow–structure interaction of an oscillating circular cylinder in the synchronization field at sub-critical Reynolds number is still an open research point, both in terms of experimental description and in terms of available numerical simulation models. The complexity of the problem is mainly due to the relevant nonlinear effects induced by the oscillating cylinder on the flow field. Evidence of this is given by the possible co-existence of different solutions to the nonstationary fluid-dynamic problem, switching from one to the other depending on minor changes in the key nondimensional parameters governing the phenomenon (nondimensional oscillation amplitude and critical velocity ratio). The tests described have been realized in air using a rigid model elastically suspended and instrumented by an on-board high frequency response pressure scanner. The instantaneous pressure distribution on a cylinder section has been measured allowing identification of different vortex shedding states and calculation of aerodynamic integral forces on the cylinder and their correlation with the motion time histories.

1. Introduction

The flow–structure interaction problem shows, in the classical circular cylinder case, a very complex phenomenology strongly dependent on the following key parameters: Reynolds number Re, mass ratio m^*, mass damping $m^*\xi_s$ (or Scruton number Sc*), nondimensional amplitude z^* and critical velocity ratio U_n (see Nomenclature). In the synchronization range in particular, there is evidence of experimentally monitored solutions characterized by very different qualitative appearance both in the wake structure and in the forces on the cylinder (Khalak and Williamson, 1999; Govardhan and Williamson, 2000). The research described here addresses the sub-critical Reynolds number range, around $\mathrm{Re} \simeq 5 \times 10^4$, which is characterized by a very large spectrum of applications. A large amount of literature, mainly focusing on the integral parameters characterizing the flow–cylinder interaction, addresses the proposed test case in terms of total instantaneous aerodynamic forces correlated with motion time histories (Carberry and Sheridan, 2001). More recently a key topic has been the study of the wake structure of free oscillations and forced oscillation tests (Carberry et al., 2004). The present researches' contribution is the measurement of the instantaneous pressure distribution on a section of the oscillating cylinder, in order to correlate the instantaneous integral forces with the motion time histories. This will give an insight into the core of the fluid-dynamic mechanism generating the forces during the vortex shedding phenomenon. As far as it is known by the authors, no attempt has been documented in literature on the instantaneous pressure distribution approach. The ongoing research is aimed at generating a reference

*Corresponding author.
E-mail address: alberto.zasso@polimi.it (A. Zasso).

0889-9746/$ - see front matter © 2007 Elsevier Ltd. All rights reserved.
doi:10.1016/j.jfluidstructs.2007.11.007

Nomenclature

D	cylinder diameter (0.2 m)
f^*	frequency ratio (f/f_N)
f	actual frequency of oscillating cylinder in the flow
f_N	natural frequency of oscillating cylinder in still water (f_s in still air)
f_s	natural frequency of oscillating cylinder in still air ($f_s = 3.25$ Hz)
T, T_s	corresponding cylinder oscillation periods
f_{vs}	vortex shedding frequency from still cylinder ($z = 0$)
f_n^*	critical frequency ratio ($f_{vs}/f \equiv U_n$)
L	cylinder length (2.0 m)
Re	Reynolds number ($\mathrm{Re} = \rho U_\infty D/\mu$)
Sc	Scruton number (Ref. Chen, 1993) $\mathrm{Sc} = 2\pi m\xi_s/\rho D^2$
Sc*	Scruton number (Ref. Simiu and Scanlan, 1996) $\mathrm{Sc}^* = m\xi_s/\rho D^2$
U_{vs}	critical free stream velocity (fD/St_{vs})
U_n	critical velocity ratio (U_∞/U_{vs})
U^*	velocity ratio ($U_\infty/f_N D$)
$(U^*/f^*)\mathrm{St}_{vs}$	x-axis parameter allowing good collapsing among water and air free response tests data $((U_\infty/(f_N D)) \cdot (f_N/f) \cdot ((f_{vs}D)/U_\infty) = f_{vs}/f = U_n)$
V^*	reduced velocity (U_∞/fD)
z	cross-flow cylinder oscillation amplitude ($\lvert z\rvert < 0.3$ m)
z^*	nondimensional displacement ($z^* = z/D$)
μ, ρ	air viscosity and density
ω, ω_s	corresponding circular frequencies of oscillating cylinder

Here we use Nomenclature generally adopted in literature (Govardhan and Williamson, 2000). The symbol f_N in water is the equivalent of f_s in air, so that we use in the following f^* indifferently as to whether $f^* = f/f_s$ or $f^* = f/f_N$, depending on the fluid flow.

data base of pressures, which will also be used for validating CFD simulations in contiguous research at Politecnico di Milano (Diana et al., 2005a,b, 2006).

2. Experimental methods review

The study of the vortex shedding effects on the oscillating circular cylinder presented in this paper utilizes the symbols listed in Nomenclature.

For the sake of coherence with the slightly different nomenclature used in literature, typically referred to as tests in water, a table of correspondence is also quoted in Nomenclature. In particular, it is worth noting that the parameter "critical velocity ratio" $U_n \equiv f_n^*$ used in the present paper coincides with the parameter $(U^*/f^*)\mathrm{St}_{vs}$ used by Govardhan and Williamson (2000). It is well accepted that this choice of coordinate allows a generalized representation with a good collapse of different sets of free response results coming from air and water tests. The experiments presented in the paper have been performed on a $D = 0.2$ m circular cylinder. It oscillates at a natural frequency $f_s = 3.25$ Hz in a narrow Reynolds number range around $\mathrm{Re} \simeq 5 \times 10^4$, allowing for a description of the vortex shedding phenomenology in the observed response range $0.85 \leqslant U_n \leqslant 1.3$.

The vortex shedding phenomenology from an oscillating cylinder is naturally described in z^* versus U_n plane, where different topologies have been observed in forced and free oscillation tests (Brika and Laneville, 1993; Carberry et al., 2004). The authors believe that the topology of the flow, and as a consequence the vortex shedding phenomenology, at a given Re and in stationary cylinder oscillations, is a function of the above-mentioned two kinematic parameters z^* and U_n. This gives the moving boundary conditions to the nonstationary fluid-dynamic problem. The most significant encountered topologies are 2S and 2P, which are involved when a freely oscillating cylinder is observed in the lock-in region. Visualization techniques show the 2S type being two oppositely signed vortices shed per oscillatory cycle. On the other hand in the 2P type two pairs of vortices are formed per cycle with each pair comprised of two oppositely signed vortices convected laterally outwards from the wake centre-line. Fig. 1 shows the response of freely oscillating cylinders represented in Williamson and Roshko (1988) map of wake modes. The present data have been compared with corresponding literature results (Feng, 1968; Govardhan and Williamson, 2000). In the diagram, progressive regime results are reported, which have been obtained by increasing the wind velocity in small steps without interrupting the cylinder oscillation, together with the final regime conditions reached by subsequent build-up transients started from rest.

A few preliminary comments should be given on the data presented in Fig. 1. The progressive regime results do not differ significantly from the build-up data in terms of maximum reached amplitudes. Some minor differences are

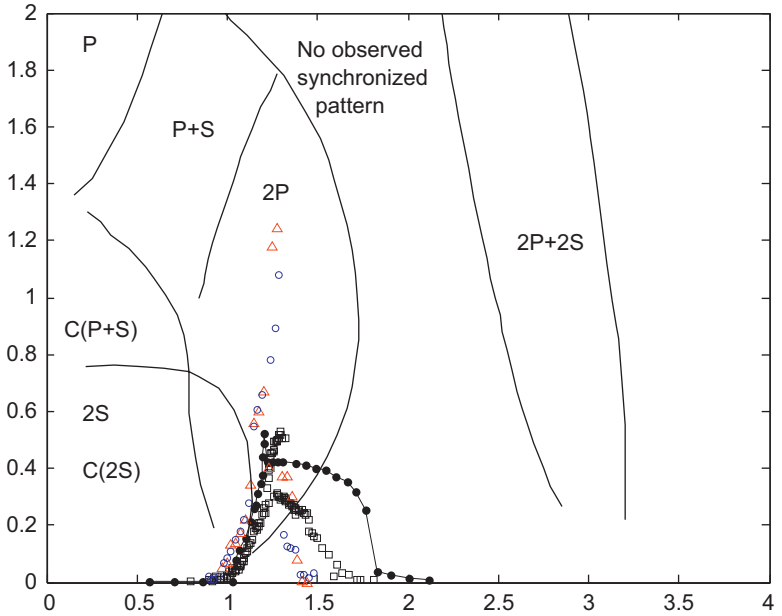

Fig. 1. Free vibration cylinder response in plane z^* versus U_n. ○, Present research progressive regimes data; △, present research build-up data (final reached regime amplitude); □, Feng (1968); ●, Govardhan and Williamson (2000).

attributed to contemporary presence of data coming from the two sets of experiments, realized with a renewed set-up and slightly different $m^*\xi_s$. It is of course well accepted that, in the case of possible hysteretical multiple solution behaviour, typical of the higher U_n region, the possibility of reaching specific locations in z^* versus U_n plane depends on the initial condition of the problem. Hence, given a specific U_n, the build-up from rest and the progressive regimes method could reach different rows of co-existent solutions. The most relevant originality of the presented data, compared with the existing literature, is the reaching of very large amplitudes $z^* \simeq 1.25$ in air tests at large mass ratio m^*, clearly belonging to the 2P "upper branch" region. It is the authors' opinion that the peculiarity of the present experiment lies in the special care devoted to realizing "ideal experimental conditions" both in terms of the two-dimensionality of the flow (large cylinder aspect ratio, very rigid model, end-plates, flow quality) and in terms of the strict control of the mechanical parameters, with specific attention to their possible dependence on the oscillation amplitude. In Table 1, m^* and $m^*\xi_s$ are quoted for the three experiments compared in Fig. 1. As shown in Fig. 2, the dependence of ξ_s on the oscillation amplitude has been considered in the present tests, resulting in a mass-damping parameter increase of a factor of three in the z^* range considered. As a consequence, for the present data, $m^*\xi_s$ matches the existing experimental results only if the largest ξ_s is taken into account. It is the authors' opinion that the disagreement in the maximum amplitudes reached could be a result of the different definition of the structural damping parameter ξ_s. The possible dependence $\xi_s(z^*)$ cannot be ignored, and a single value of $m^*\xi_s$ for a set of results spanning over a large z^* range could be misleading. At the same time, the extension of the present experimental response curve on U_n axis, is much lower than the Govardhan and Williamson (2000) data and also lower than the Feng (1968) results. No clear explanation is available for that disagreement, and further research is needed.

The modal mass per unit length m takes into account the contribution of all the oscillating suspended fittings. The structural nondimensional damping ξ_s has been estimated from decays in still air, accounting for its dependence on the oscillation amplitude z^*. A specific analysis has been performed in order to separate the damping contribution that is due to the mechanical fittings, from the one attributed to the viscous effects in still air, evaluated from analysis of the unsteady pressures measured on the oscillating cylinder. The results indicate that, at large z^*, the most relevant contribution is the mechanical one, and that by comparison the viscous effects in still air are negligible.

The mechanical modelling of the cylinder undergoing sinusoidal oscillations at circular frequency ω, due to flow interaction, is clarified by the introduction of further quantities summarized in Table 2. Specific attention is given to an energy balance approach.

The instantaneous cross-flow aerodynamic force on the cylinder is given by the integration of the instantaneous pressure distribution $C_P(\vartheta, t)$ along the measured cylinder section, where ϑ is the angle between the pressure measuring location and the free-stream wind direction (more details can be found in Zasso et al., 2005). The ongoing research

Table 1
Structural parameters: nomenclature and nondimensional groups

m	modal mass per unit length	$m = 5.5\,\mathrm{kg/m}$
m^*	mass ratio	$m^* = m/(\pi\rho D^2/4) \simeq 142$
ξ_s	structural nondimensional damping	$3 \times 10^{-4} < \xi_s(z^*) < 1.7 \times 10^{-3}$
$m^*\xi_s$	mass-damping parameter	$4.4 \times 10^{-2} < m^*\xi_s < 2.4 \times 10^{-1}$
Sc	Scruton number	$0.22 < \mathrm{Sc} < 1.22$
Sc	Scruton number (Chen, 1993)	$\mathrm{Sc} = 2\pi \frac{m\xi_s}{\rho D^2}$
Sc*	Scruton number (Simiu and Scanlan, 1996)	$\mathrm{Sc}^* = \frac{m\xi_s}{\rho D^2}$
ξ_T	build-up exponential trend	$z^*(t) \simeq z_o^* \, \mathrm{e}^{\omega_s \xi_T t} \sin(\omega t)$
Fig. 1 literature experiment □	Feng (1968)	$m^* = \mathcal{O}(100)$
Fig. 1 literature experiment □	Feng (1968)	$m^*\xi_s = 0.25$
Fig. 1 literature experiment ●	Govardhan and Williamson (2000)	$m^* = 320$
Fig. 1 literature experiment ●	Govardhan and Williamson (2000)	$m^*\xi_s = 0.251$

The specific values of mass-ratio and mass-damping parameters of the literature results reported in Fig. 1 are also quoted.

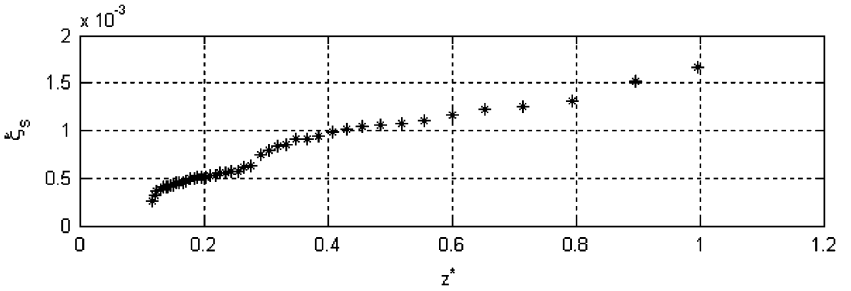

Fig. 2. Experimental trend ξ_s versus z^* from free oscillation tests in still air.

Table 2
Interaction force and energy parameters: nomenclature and nondimensional groups

$F_{Az}(t)$	instantaneous cross-flow aerodynamic force on the cylinder per unit length	$F_{Az}(t) = \frac{1}{2}\rho U_\infty^2 \frac{D}{2} \int_0^{2\pi} C_P(\vartheta, t) \sin(\vartheta)\, \mathrm{d}\vartheta$
$C_D(t)$, $C_L(t)$	drag and lift coefficients	$F_{Az}(t) = \frac{1}{2}\rho U_\infty^2 D C_L(t)$
F_{Az1}	amplitude of the first harmonic cross-flow aerodynamic force in stationary oscillation	$F_{Az1} = \left\lvert \frac{1}{T} \int_{-T/2}^{T/2} F_{Az}(t)\, \mathrm{e}^{\mathrm{i}\omega t}\, \mathrm{d}t \right\rvert$
C_{L1}	amplitude of the first harmonic lift coefficient in stationary oscillation	$F_{Az1} = \frac{1}{2}\rho U_\infty^2 D C_{L1}$
z_1^*	amplitude of the first harmonic nondimensional displacement in stationary oscillation	$z_1^* = \left\lvert \frac{1}{T} \int_{-T/2}^{T/2} z^*(t)\, \mathrm{e}^{\mathrm{i}\omega t}\, \mathrm{d}t \right\rvert$
φ_{1Lz}	phase of the first harmonic cross-flow aerodynamic force (referred to z^*)	$F_{Az}(t) = F_{Az1} \sin(\omega t + \varphi_{1Lz}) + \cdots$
$\overline{W}_u$	average power input from the flow on the unit cylinder section	$\overline{W}_u = \frac{1}{nT} \int_0^{nT} F_{Az}(t) \cdot \dot{z}(t)\, \mathrm{d}t$
$\overline{W}_u^*$	nondimensional power input from the flow on the unit cylinder section	$\overline{W}_u^* = \frac{1}{\rho} \frac{\overline{W}_u}{D^4 \omega^3}$
$\overline{W}_{\mathrm{Norm}}$	normalized power input from the flow on the unit cylinder section	$\overline{W}_{\mathrm{Norm}} = \frac{\overline{W}_u}{D^4 f^3}$
t^*	nondimensional time t^*	$t^* = t \frac{U_\infty}{D}$
t_n	nondimensional time t_n (number of periods)	$t_n = t/T$
ω_s^*	nondimensional circular frequency (in still air)	$\omega_s^* = \omega_s D/U_\infty = 2\pi\, \mathrm{St}_{vs} \frac{1}{f^*} \frac{1}{U_n}$

focuses on the correlation analysis between different measurement sections positioned along the cylinder as quoted in Zasso et al. (2006). It is possible to confirm from direct measurements, as far as present research data are concerned, that a very high (close to unity) correlation is attributed to the pressure distribution along the cylinder, at least in the

case of large post-transition oscillations. A lower correlation could be expected at low oscillation amplitudes and in the case of nonsynchronized vortex shedding.

The equation of motion of the circular cylinder is assumed to be that of a single degree of freedom rigid body oscillating in cross-flow and is simply written as follows, with $C_L(t)$ being representative of the flow-cylinder unsteady interaction force:

$$\frac{\mathrm{d}^2 z^*}{\mathrm{d}t^{*2}} + 2\xi_s \omega_s^* \frac{\mathrm{d}z^*}{\mathrm{d}t^*} + \omega_z^{*2} z^* = \frac{2}{\pi}\frac{1}{m^*} C_L(t). \tag{1}$$

Due to the dependence of the interaction force on the system state and on the critical velocity ratio U_n, the most rigorous general representation of Eq. (1) is in the form of (2), where $C_L(t)$ is an implicit function of the state z^* and its derivatives, as well as of U_n:

$$\frac{\mathrm{d}^2 z^*}{\mathrm{d}t^{*2}} + 2\xi_s \omega_s^* \frac{\mathrm{d}z^*}{\mathrm{d}t^*} + \omega_s^{*2} z^* = \frac{2}{\pi}\frac{1}{m^*} C_L\left(\frac{\mathrm{d}^2 z^*}{\mathrm{d}t^{*2}}, \frac{\mathrm{d}z^*}{\mathrm{d}t^*}, z^*, U_n\right). \tag{2}$$

The strongly nonlinear dependence of the interaction force on the system state is responsible for cylinder aeroelastic response with possible substantial changes in the structural modal parameters (e.g. the fluid-added mass contribution) or even showing hysteretic jumps in the lock-in region. Considering that the nondimensional circular frequency ω_s^* can be written as

$$\omega_s^* = 2\pi\,\mathrm{St}_{vs}\frac{1}{f^*}\frac{1}{U_n}, \tag{3}$$

and considering that f^* (the ratio between the actual oscillation frequency of the cylinder in the fluid flow and the oscillation frequency in still fluid) is typically dependent on the mass ratio m^*, U_n and z^*, it can be argued that the response z^* of the cylinder should just be a function of the following fundamental parameters: the critical velocity ratio U_n, mass ratio m^* and nondimensional damping ξ_s (or in an equivalent way, mass damping $m^*\xi_s$):

$$z^* = z^*(U_n, m^*, m^*\xi_s). \tag{4}$$

In other words the mechanical parameters governing the response, (mass damping $m^*\xi_s$ and the mass ratio m^*) work together and independently, so that the mass damping parameter alone (or Scruton number) cannot be fully representative of the system mechanics. As a consequence, the most appropriate representation of the response z^* should be a three-dimensional plot giving families of surfaces z^* as a function of U_n and m^*, having assumed the mass damping parameter $m^*\xi_s$ as the parameter characterizing each specific surface of the family.

With this assumption, the usual representation in z^* versus U_n plane of response curves obtained from systems having the same $m^*\xi_s$ but different m^* are projections on (z^*, U_n)-plane of curves given by the intersection of z^* surface with different planes $m^* = m_o^*$. It follows that, although $m^*\xi_s$ is the same, the response curves of the two systems are expected to be different if the mass ratio m^* is not the same. In other words, even if the representation on (z^*, U_n)-plane gives a good collapse of water and air tests, different curves will still be expected from air and water tests having the same mass damping but very different mass ratios.

With simple considerations on the harmonic function properties, assuming the nomenclature given in Table 2, the power input due to fluid-dynamic interaction is written as

$$\overline{W_u} = \tfrac{1}{2} F_{Az1}\omega z \sin(\varphi_{1Lz}), \tag{5}$$

representing an estimate of the power input per cylinder unit length, averaged over a number of full periods of stationary amplitude oscillations. In case of a build-up trend (very low values of exponential trend are considered to be in the order of $\xi_T < 5\times 10^{-3}$), the interaction force component in phase with the cylinder velocity can be written as

$$F_{Az1}\sin(\varphi_{1Lz}) = \xi_s 2m\omega_s\omega z + \xi_T 2m\omega_s\omega z, \tag{6}$$

accounting for the structural mechanical dissipation and the kinetic energy derivative. In air tests, or more generally at high m^*, ω can be assumed to be equal to ω_s so the general expression of the power input due to flow–structure interaction in steady oscillations, and/or during build-up oscillations, has the following simple expression, clarifying the role of the Scruton number Sc*:

$$\overline{W_u^*} = z^{*2}\left(\mathrm{Sc}^* + \frac{m\xi_T}{\rho D^2}\right). \tag{7}$$

The expression shows a linear dependence of the nondimensional power input on the Scruton number and a quadratic dependence on the nondimensional oscillation amplitude. On the basis of energy balance considerations,

while the forced oscillation method experiments allow us, in principle, to cover the whole z^* versus U_n plane, the free oscillation method results are limited in the regions defined by $\overline{W_u} > 0$. A limitation in the regions allowed to be explored is then intrinsically present in the free motion method. Also the most significant cases of real life applications are covered, excluding very peculiar and limited situations where a cylinder section is driven into regions where the aerodynamic average power input is negative, by an external force. As a consequence, the representation in the plane z^* versus U_n shows sets of possible power balanced configurations, where the positive aerodynamic power input is balanced by the structural dissipations, resulting, at fixed m^*, in families of different response curves depending on the mass damping parameter $m^*\xi_s$. As a general rule, increasing amplitudes z^* are reached with decreasing $m^*\xi_s$. It is possible to assume the existence of a maximum amplitude $z^*(U_n, m^*)$ response curve limit defined by $\overline{W_u} = 0$ which is the borderline separating positive from negative flow–cylinder interaction power input. Very low values of nondimensional damping ξ_s have been realized in the experimental set-up, for the purpose of extending the explored z^* versus U_n region towards the largest z^* amplitudes and the wider U_n synchronization interval. Finally, a few words should be said concerning the comparison between the results of experiments in air and in water (Govardhan and Williamson, 2000). Although the key aerodynamic parameters Re, z^* and U_n, and the key flow–structure interaction parameter Sc* were the same, the experiments in air typically reach very low Sc* values relying on very low ξ_s, while the experiments in water typically rely on very low mass ratio m^*. Therefore, in the water case, the added mass fluid-dynamic contribution has significant effects on the interaction problem, due to very large $\rho\pi D^2/4$ values, comparable to the cylinder mass per unit length, whereas in air testing, these effects are generally negligible, due to the very high m^* values, no significant frequency shifts due to the air added mass effects are expected in air tests. Specifically in the present experiment, the difference between the actual cylinder frequency of oscillation in the flow f and the cylinder oscillation frequency in still air f_s is negligible, hence giving $f_s = f$. On the other hand, the added mass effect, at low m^*, is dominant and can significantly affect the results in the water experiments. Comparisons of the air–water experiments should, therefore, consider these circumstances. The dynamic pressure distribution approach has been selected in order to define the fundamental basis of the aerodynamic force generation. This allows for an in-depth understanding of the fluid-dynamic phenomenon and possible comparisons with literature data related to visualization of the near wake flow topology, and to ongoing CFD studies (Willden, 2006).

3. Model and experimental set-up

The model was a smooth acrylic fibre cylinder with an aspect ratio $A_R = 10$ and two large end-plates located at the extremities in order to realise two-dimensional (2-D) flow conditions. The large test-section size (14 m × 4 m) allowed us to suspend the model from the wind tunnel walls by means of two tensioned 14 m wires passing inside the cylinder and realizing a constraint system acting as a vertical spring with linear behaviour for oscillation amplitudes up to $z^* \simeq 1.3$ (see Fig. 3). Possible coupling of horizontal and torsional motion was avoided through sufficiently wide separation between the horizontal–vertical and the torsional–vertical frequencies. In Nomenclature and in Table 1 all the fundamental mechanical characteristics of the oscillating system are summarized. With reference to the cross-flow (vertical motion) natural frequency in still air $f_s = 3.25$ Hz, the critical free-stream velocity was $U_{vs} = 3.6$ m/s, corresponding to a Strouhal number equal to $\mathrm{St}_{vs} = 0.18$. The Strouhal number value has been defined through higher speed tests with the cylinder far from the synchronization region.

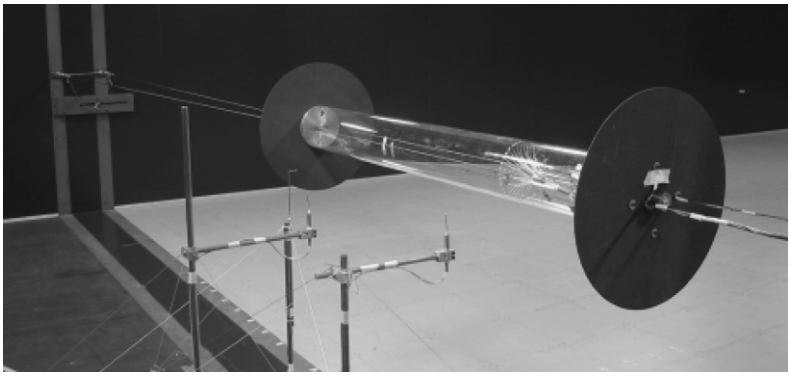

Fig. 3. Rigid oscillating cylinder model in the Politecnico di Milano Boundary Layer Wind Tunnel.

All tests were performed in a narrow sub-critical Reynolds number range ($\mathrm{Re} \simeq 5 \times 10^4$) in smooth flow conditions. The incoming free-stream flow characteristics were monitored through a three-component high frequency pressure probe, showing quite uniform along-wind turbulence intensity $I_u \simeq 2.0\%$. The deviation $\Delta U_\infty / U_\infty$ of the average wind speed along the cylinder span is limited to the order of $\Delta U_\infty / U_\infty \simeq \pm 2.5\%$. The model has been instrumented with 32 pressure taps distributed on a cylinder section. The taps were connected to a high-speed scanner allowing high resolution measurements of the fluctuating pressure field and mean components in the time domain. The pressure scanner has been installed inside the model with short pneumatic connections to the pressure taps. This solution guarantees a high frequency response to the tubing system. The peak acceleration is equal to $\ddot{z} \simeq 100\,\mathrm{m/s^2}$ given $z^* \simeq 1.2$ at a frequency $f_s = 3.25\,\mathrm{Hz}$ (see Fig. 4). Due to the large accelerations encountered, many tests have been performed in order to estimate possible inertial effects on the pressure transducers, recognizing finally that these effects can be neglected through an appropriate measurement set-up (Zasso et al., 2005). The cylinder dynamics was monitored through miniaturized accelerometers, two of which were positioned at the cylinder edge sections measuring the vertical motion and one of which positioned in the middle of the cylinder measuring the horizontal in-line motion. The analysis of the acceleration data highlighted a pure vertical motion of the cylinder. As the analysis of the relative phase between

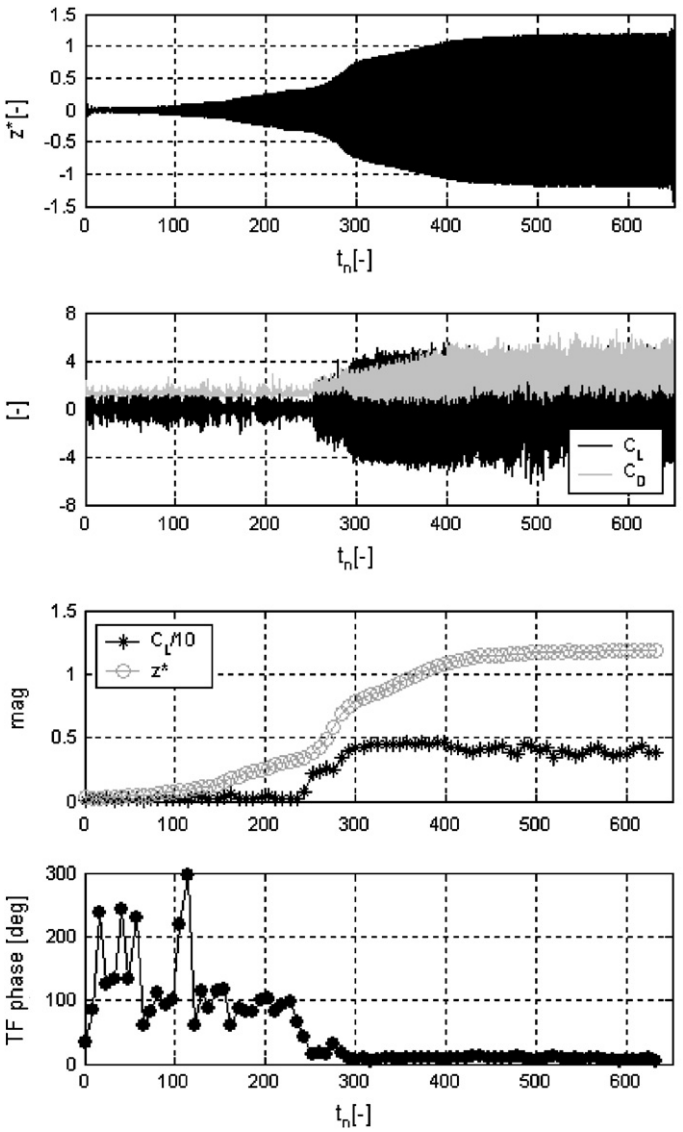

Different growth trends are shown by the build-up due to differences between fluid-interaction power input and mechanical dissipations. One can observe $z^* \simeq 1.2$ reached by a high mass ratio system, $m^* \simeq 142$. Being $m^*\xi_s \simeq 0.25$ the mass damping at max amplitude.

As an effect of the transition at $t_n \simeq 225$ $C_D(t_n)$ and $C_L(t_n)$ show a dramatic increase reaching peak values greater than 5 with an almost sinusoidal time history perfectly synchronized with the cylinder oscillations ($C_D(t_n)$ having double frequency).

The time-frequency analysis of the build-up clearly identifies the transition between "first state" and "upper branch" at $225 \le t_n \le 260$. The "first state" is characterized by low C_{L1} and phase $\varphi_{1Lz} \simeq 100°$, while the "upper branch" shows very large $C_{L1} \simeq 5$ and positive but almost zero phase φ_{1Lz}. Larger amplitudes $z_1^* \simeq 0.32$ are needed for transition at $U_n = 1.25$ compared to the $U_n = 1.17$ case where just $z^* \simeq 0.2$ are needed

Fig. 4. Build-up at $U_n = 1.25$ showing the clear transition from a "first state" to the "upper branch".

fluid-dynamic interaction force and cylinder oscillation is a fundamental topic of the present research, specific care was devoted to verify that pressure and acceleration signals were synchronized. For this purpose a direct check in the acquired data of possible time shifts between the different measure chains (pressures and accelerations) has been verified by means of impulsive events concurrently detected by all the measured channels on the cylinder. A hot-wire anemometer and two high frequency response (2 kHz) three-component pressure probes were positioned downstream the cylinder for studying the wake structure. The analysis of the wake flow monitoring, however, is not an object of the present paper.

4. Reference time histories analysis: integral quantities

The available time history records of steady and transient oscillations were organized in a data base including pressures, cylinder accelerations, and wake flow three-component velocities. The above-mentioned data were monitored varying the critical velocity ratio U_n as an independent parameter in the response range $0.85 \leqslant U_n \leqslant 1.3$. The analysis of the instantaneous pressure field distribution, together with the monitoring of some significant integral parameters , allowed us to clearly recognize some of the states expected in the vortex shedding phenomenology. The most significant time histories are shown for this purpose, summarizing the three fundamental states encountered. In the research technique adopted, not only steady oscillations have been considered, but also transient build-up oscillations at fixed U_{nO}, with amplitude varying from $z^* = 0$ to a steady level regime at a very low equivalent exponential trend ξ_T (maximum encountered $\xi_T \leqslant 5 \times 10^{-3}$). During the build-up transients the state of the system could be identified as a point moving along the straight line $U_n = U_{nO}$ in $\{z^*, U_n\}$ space delimited underneath the system response curve specific to the selected mechanical parameters m^* and $m^*\xi_s$. Due to the very low ξ_T levels encountered, a hypothesis of quasi-steady conditions is implied, allowing us to study the unsteady pressure distribution, the interaction fluid-dynamic force and the power input as functions of the state $\{z^*, U_n\}$. As an example, Fig. 5, for $U_n = 1.17$, shows the nondimensional oscillation $z^*(t_n)$ and the instantaneous total drag $C_D(t_n)$ and lift $C_L(t_n)$ coefficients on the section as functions of the nondimensional time t_n. The lift and drag components of the instantaneous aerodynamic force on the section are conventionally assumed to be parallel and orthogonal to the direction of oscillation of the cylinder that is cross-flow. In the same diagram, a time-frequency analysis of $C_L(t_n)$ and $z^*(t_n)$ is presented, showing their harmonic components C_{L1}, z_1^* and relative phase φ_{1Lz} (lift force minus cross-flow displacement phases) related to the oscillation frequency of the cylinder, as a function of nondimensional time. In the following, due to the strictly mono-harmonic cross-flow cylinder oscillation, z^* and z_1^* are used as equivalent notations. F_{Az1}, the only harmonic component of the lift force responsible for possible aerodynamic power input from the flow, is hence represented in terms of nondimensional magnitude C_{L1} and relative phase φ_{1Lz} together with the corresponding displacement harmonic component of the oscillating cylinder. Each dot symbol on the time-frequency analysis diagram corresponds to an average number of 10 oscillation cycles of the cylinder, having quite constant amplitude due to the very low equivalent exponential trend ξ_T. In these 10 cycles, an average estimate of the above-mentioned parameters is given through FFT analysis. Finally, the power input $\overline{W_u}$ is represented as a function of t_n. All the above-mentioned integral quantities have been evaluated through space integration of the instantaneous pressure time histories, generating equivalent drag and lift coefficient time histories, and finally evaluating the instantaneous $W_u(t)$ and average $\overline{W_u}$ power input from the definition given in Table 2. The instantaneous velocity time history was calculated by integration of the acceleration signal (through frequency domain FFT approach, filtering the possible undesired low frequency noise drifts). Detailed reference of the power input analysis can be found in Zasso et al. (2005), where the results of the pressure integration method are compared with those from the usual build-up time history analysis. Regular growing amplitude $z^*(t_n)$ oscillations are shown at $U_n = 1.17$, reaching typical values of $\xi_T \simeq 5 \times 10^{-3}$ with equivalent exponential trend finally limited at $z^* \simeq 0.6$.

On the other hand, the instantaneous $C_L(t_n)$ and $C_D(t_n)$ plots show very irregular behaviour in the initial stages, with a sudden transformation to a very regular, large amplitudes regime starting at $t_n \simeq 80$, corresponding to $z^* \simeq 0.2$. The time-frequency analysis shown in C_{L1}, z_1^* and φ_{1Lz} plots gives a clear interpretation of the phenomenon. Two different states are evident: the "first state", characterized by $\varphi_{1Lz} \simeq 90^\circ$ and very low C_{L1} values, and the "second state" showing very low phases $\varphi_{1Lz} < 10^\circ$ and very large lift $C_{L1} \simeq 4$. The transition from "first state" to "second state" is marked by a sudden drop of the phase φ_{1Lz} happening in the range $0.2 < z_1^* < 0.35$ and by a simultaneous and sudden increase of the synchronized lift C_{L1}. A thorough data base enquiry (results shown in Fig. 6) allowed us to demonstrate that the transition is a function of z_1^*, happening at larger z_1^* values as a function of increasing critical velocity ratio U_n. The power input analysis shows quite low $\overline{W_u}$ values in the "first state", then a maximum increasing trend corresponding to the transition region, reaching the largest values at the end of the increasing amplitude range and stabilizing around $\overline{W_u}$ values required by the structural damping specific of the regime amplitudes. The power input values estimated by instantaneous pressure integration has always been found to be in agreement with the estimate given by Eq. (6)

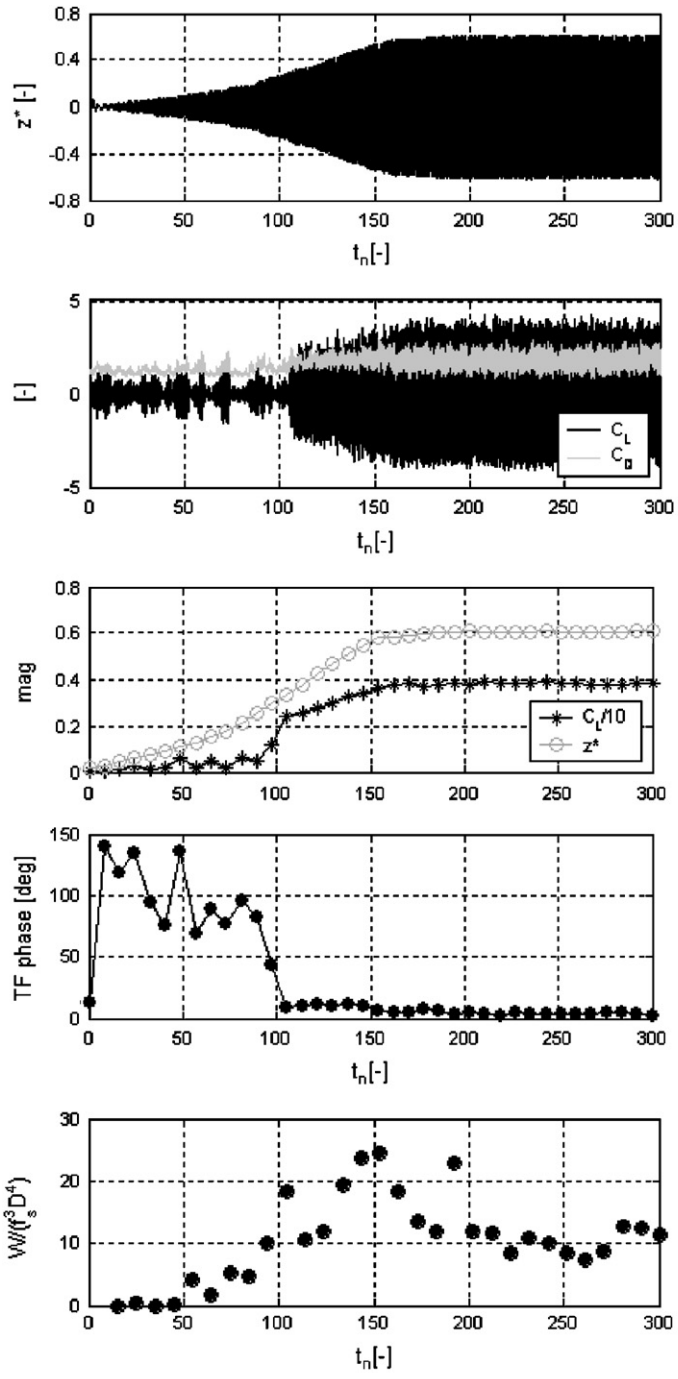

Nondimensional amplitudes $z^*(t_n)$ function of non-dimensional time t_n (oscillation cycles).

Time histories $C_D(t_n)$ and $C_L(t_n)$ show a "first state" not synchronized vortex shedding and a transition to the "upper branch" at around $t_n \approx 80$. "Upper branch" is characterized by fully synchronized and by high values of interaction force.

The build-up time-frequency analysis is evaluated on the basis of 10 cycles. Transition is clearly shown around $t_n \approx 80$ with an increase of a factor of 10 of the synchronized lift component C_{L1} and an abrupt jump of the phase from $\varphi_{1Lz} \approx 90°$ ("first state") to $\varphi_{1Lz} \approx 0$ ("upper branch"). At $U_n = 1.17$ $z^* \approx 0.2$ is needed to start transition.

Moving-average over 10 cycles of the flow-interaction instantaneous power input. The conventional normalized representation is given:

$$\overline{W}_{Norm} = \frac{\overline{W}_u}{D^4 f_s^3}$$

The inertial contribution of growing amplitude causes maximum power input value not at maximum amplitude z^*.

Fig. 5. Build-up at $U_n = 1.17$ showing the clear transition from a "first state" to a "second state".

accounting for both dissipative and incremental kinetic energy terms, where the dependencies $\xi_s(z^*)$ and $\xi_T(z^*)$ have been considered (Zasso et al., 2005).

The "second state" is clearly characterized by a perfectly synchronized sinusoidal large amplitude $C_L(t_n)$, with a phase φ_{1Lz} positive but approaching zero, justifying, at very large values of both C_{L1} and z_1^*, the limited power input required by the very low $\xi_s(z^*)$. Fig. 7 clearly shows, in terms of time histories, the typical "second state" configuration, where the cross-flow force is perfectly locked to the cylinder oscillation frequency f_s.

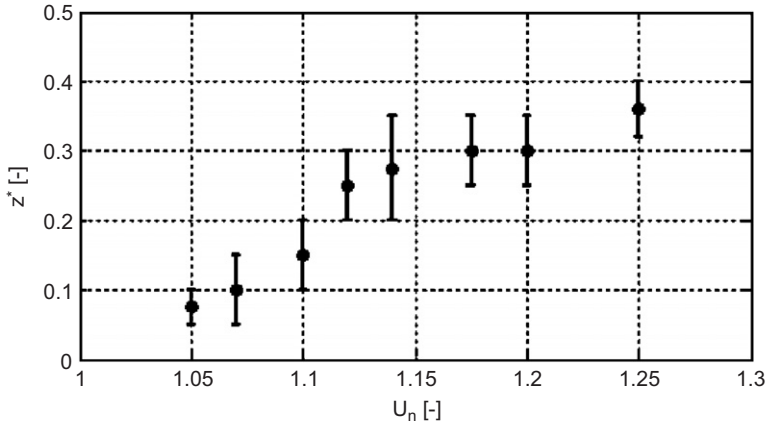

Fig. 6. "First state" to "upper branch" transition and estimated relationship $z^* > z^*_{\text{threshold}}(U_n)$.

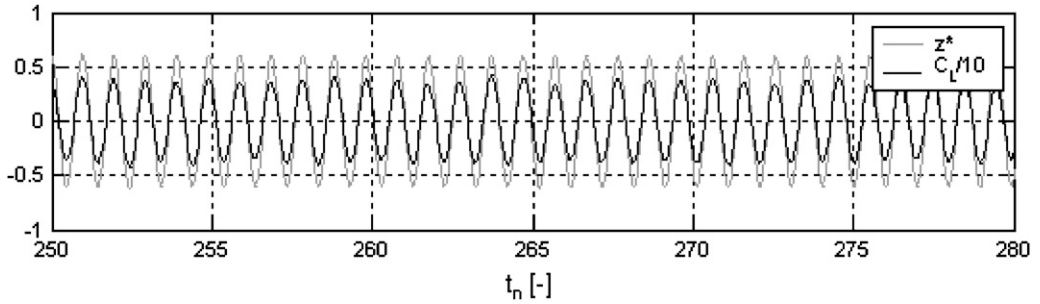

Fig. 7. Steady regime oscillations at $U_n = 1.17$ showing vortex shedding typology referred as "second state", perfectly synchronized with the cylinder oscillations.

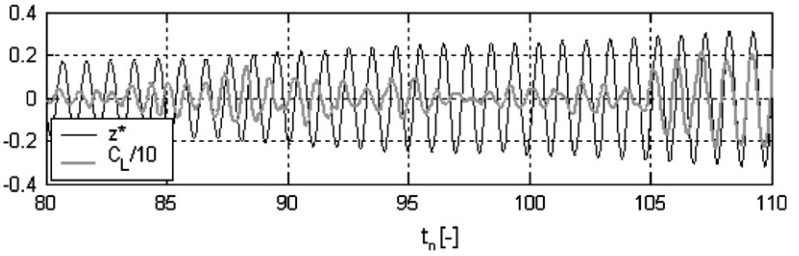

Fig. 8. Build-up low oscillation amplitude initial conditions at $U_n = 1.17$ showing a clear situation of not synchronous vortex shedding in the "first state".

On the other hand, the "first state" is characterized by very low C_{L1} and very large φ_{1Lz} values. The C_{L1} component approaching zero is very efficient in terms of power input, thanks to the phase $\varphi_{1Lz} \simeq 90^\circ$. At the same time the $C_L(t_n)$ time history of the "first state" also shows quite strong, superimposed, irregular vortex shedding effects, much larger than the quoted C_{L1} values. A detailed analysis, as shown in the zoomed $C_L(t_n)$, $z^*(t_n)$ plot of Fig. 8, allowed us to understand that in the "first state" there is always evidence of an irregular (not continuous) vortex shedding. This is not synchronised with the cylinder oscillations and happens at a frequency f_{vs} a bit higher than the structural oscillation frequency f_s of the cylinder, with f_{vs}/f_s equal to $U_n = U_\infty / U_{vs}$.

Due to the frequency difference, it is clear that no average power input is given by the nonsynchronous vortex shedding and only the very small but quite stable and very phase-effective C_{L1} component is responsible for the increasing amplitude trend in the "first state". As shown in Fig. 9, quoting the spectrum of the $C_L(t_n)$ time history, the "first state" always shows two components in the C_L spectrum: the one at frequency f_{vs} representative of the Karman

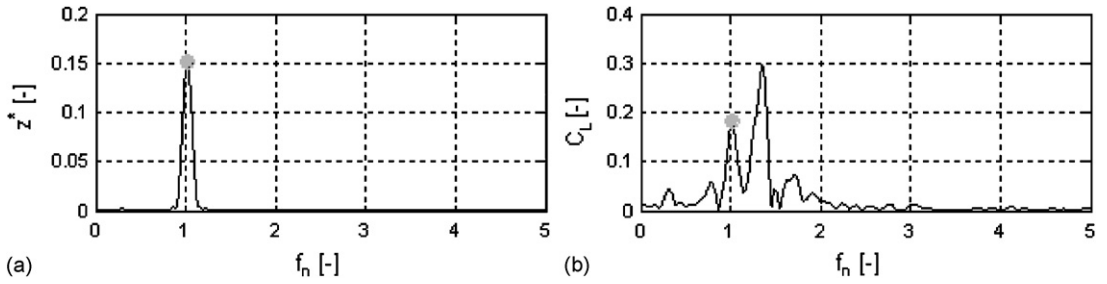

Fig. 9. $U_n = 1.17$: spectra of (a) $z^*(t_n)$ and (b) $C_L(t_n)$ in the "first state", $55 < t_n < 75$, showing the mono-harmonic cylinder oscillation and the two flow-induced forcing components, having defined $f_n = f/f_s$.

vortex shedding and the other at frequency f_s representative of a cross-flow forcing synchronized with the cylinder motion. The transition phenomenon shows a sudden regularization of the $C_L(t_n)$, an abrupt jump in $C_L(t_n)$ values by a factor of ten and simultaneously a phase jump from $\varphi_{1Lz} \simeq 90^\circ$ to φ_{1Lz} just above zero values. The z^* threshold value, when this transition occurs, is a function of and increases with U_n. Although a direct check of the vortex shedding topology was not possible (no visualization techniques were used during the pressure experiments), there are good reasons to believe that the so-called "second state" is the "upper branch" state, characterized by 2P vortex shedding and thoroughly described in the literature by Govardhan and Williamson (2000). In fact, Fig. 1 shows that the large z^* regime measured response is clearly positioned in the 2P region. Moreover, the "post-transition" conditions, in terms of both interaction force phase φ_{1Lz} and peculiar pressure distribution, as shown in the following plots, are very stable up to the very large $z^* \simeq 1.25$ amplitude where only the "upper branch" has been described in literature. In Khalak and Williamson (1999) the $\varphi_{1Lz} \simeq 0^\circ$ phase between interaction force and cylinder displacement characteristic of the "upper branch" is clearly quoted. It is difficult to assign a defined vortex topology to the so-called "first state". The simultaneous presence in the force of two frequencies, f_{vs} and f_s, is in agreement with the "initial branch" description given by Khalak and Williamson (1999); f_{vs} corresponds to Karman vortex shedding and f_s is synchronized with the cylinder oscillations. The distinctive feature of the "first state" is the clear values of $\varphi_{1Lz} \simeq 90^\circ$ of the synchronized component phase; this is not in agreement with the quoted $\varphi_{1Lz} \simeq 0^\circ$ phase of the "initial branch". As in Khalak and Williamson (1999), we measure $\varphi_{1Lz} \simeq 0^\circ$ in the low amplitude regime conditions represented in Fig. 10, so that the "initial branch" and corresponding 2S vortex shedding topology should refer only to those lower amplitude regime points. We could finally argue that in the region beneath the regime response a transition from an underlying "first state" is defined. This "first state" region being characterized by superposition of Karman vortex shedding over a synchronized force component having phase values around $\varphi_{1Lz} \simeq 90^\circ$ (see Figs. 9 and 5).

Similar considerations also hold true for the following build-up shown in Fig. 4, recorded at $U_n = 1.25$ and reaching $z^* \simeq 1.2$ oscillation amplitudes. The time-frequency analysis of the lift coefficient $C_L(t_n)$ is shown in the 3-D plot of Fig. 11, where a different nature of the flow–structure interaction in the "first state" and "second state" or "upper branch" is clearly underlined by the low amplitude two-frequency zone of the "first state" and the large amplitude single frequency of the "upper branch". The transition is clearly marked by the sudden change happening at $t_n \simeq 225$ as soon as the oscillation amplitude reaches $z^* \simeq 0.32$.

In Fig. 4 one can observe a clear jump of φ_{1Lz} and simultaneously a transition to the "upper branch" with values of the aerodynamic nonstationary lift approaching $C_{L1} \simeq 5$ and a significant increase in the average $C_D(t_n)$ at $225 \leqslant t_n \leqslant 260$, corresponding to the range $0.32 < z^* < 0.4$. A clear and stable "first state" configuration is also documented up to $t_n < 225$, $z^* < 0.32$, confirming the tendency to postpone the transition at larger z^* values increasing U_n.

Another build-up is shown in Fig. 12 at $U_n = 1.28$. A steady-state condition is, in fact, reached between $400 < t_n < 550$ showing very low C_{L1} values at non-negligible oscillation amplitudes $z^* \simeq 0.4$, with intermediate phase levels $\varphi_{1Lz} \simeq 50^\circ$. The amplitudes are lower than the ones reached in the subsequent time evolution where the oscillation switches suddenly to the "upper branch" regime at $z^* \simeq 1.25$ and the C_{L1} component grows to $C_{L1} > 4$. The authors believe that this unstable switching between an intermediate stable state and the "upper branch" corresponds to very similar behaviour described in literature by Sarpkaya (2004), Govardhan and Williamson (2000) and Khalak and Williamson (1999). The possible co-existence of two different regime branches ("upper branch" and "lower branch"), is, in fact, well known in the higher U_n range, with nonlinear phenomena of hysteresis and unstable switching. The encountered stable state is believed to be an intermediate configuration between the "upper branch" and the "lower branch". Fig. 13 gives us a build-up characterizing the "lower branch" at the far right limit of the response curve at $U_n = 1.3$. The amplitudes can still reach non-negligible values, $z^* \simeq 0.4$, but very low C_{L1} values of

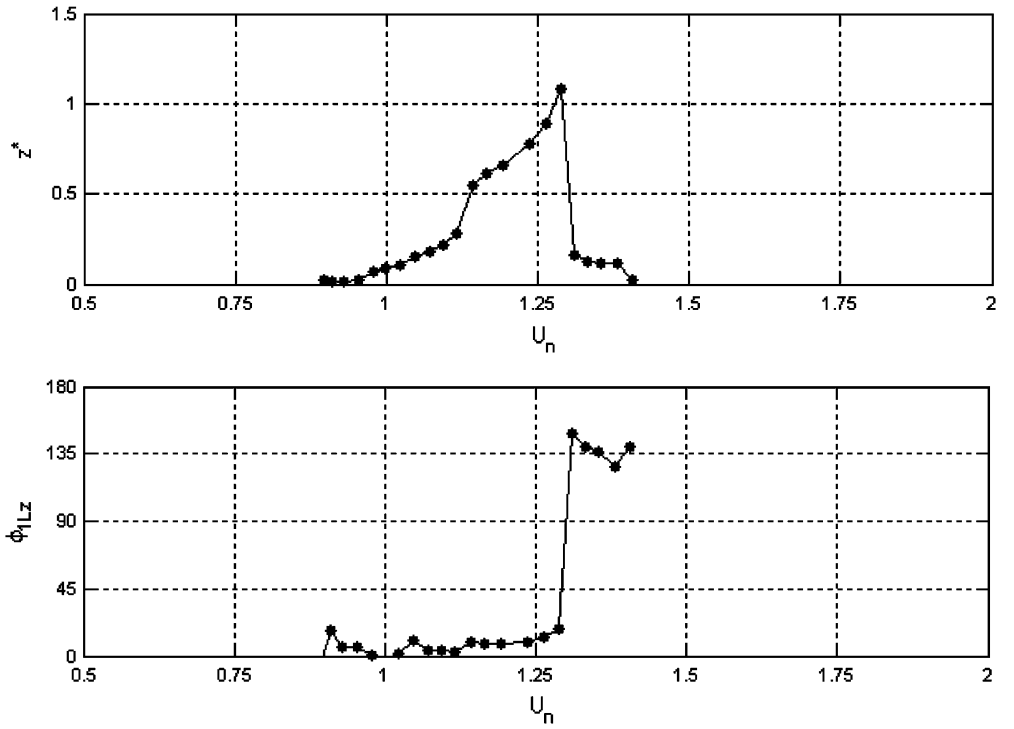

Fig. 10. Free vibration cylinder response in the plane z^* versus U_n (present research progressive regimes data). Response amplitude z^* and phase φ_{1Lz} of the first harmonic cross-flow aerodynamic force (referred to z^*).

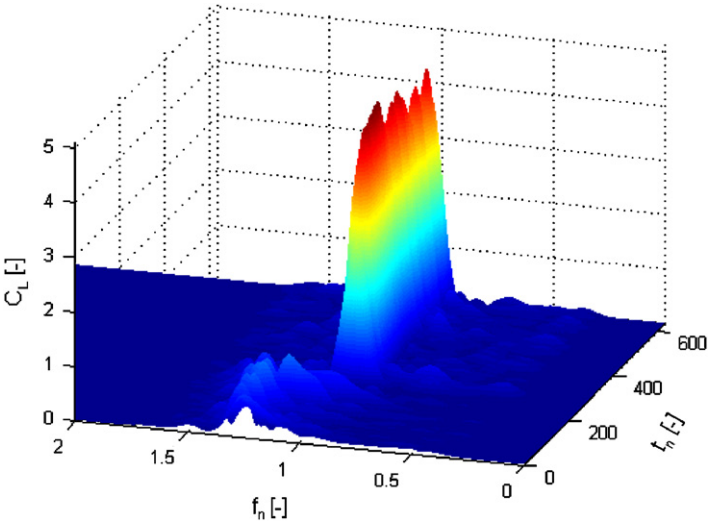

Fig. 11. $U_n = 1.25$: 3-D plot of the $C_L(t_n)$ time-frequency analysis, having defined $f_n = f/f_s$.

the aerodynamic force synchronized with the oscillation are found ($C_{L1} < 0.2$), characterized by a very effective phase $50^\circ < \varphi_{1Lz} < 150^\circ$.

This seems to confirm once again the tendency towards an increase of the phase with an increase of U_n, also showing some quite stable configuration at $120^\circ < \varphi_{1Lz} < 180^\circ$ as in the region $t_n > 600$. A close look at the time histories shows that quite strong vortex shedding is present, with instantaneous relevant values $C_L(t_n) > 1$ but not synchronous with the oscillation specifically characterized by a higher frequency, thereby giving no contribution to the average power input $\overline{W_u}$.

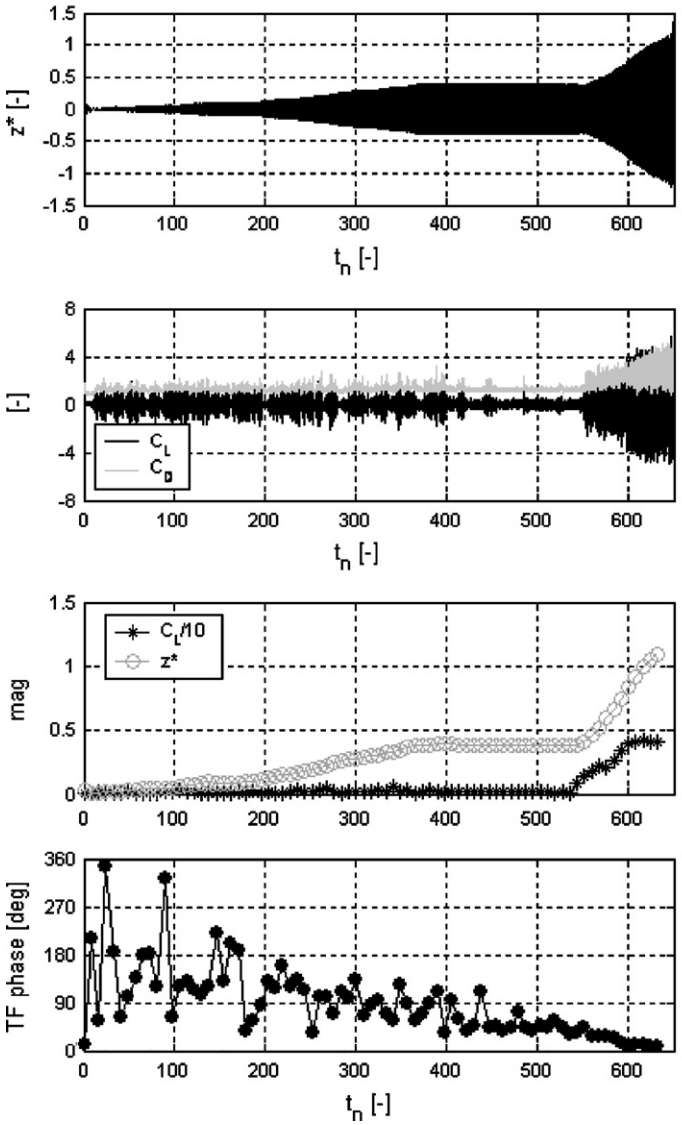

Low growth $\xi_T < 10^{-3}$ trend measured at $U_n = 1.28$ resulting in a stable steady state region of ≈ 200 cycles ($360 \le t_n \le 550$) with subsequent transition to "upper branch". This stable state is believed to be an intermediate configuration between the "upper" and "lower branch".

Not synchronous vortex shedding is clearly marked by $C_D(t_n)$ and by $C_L(t_n)$ superimposed on a low amplitude synchronized force component. After transition at $t_n \ge 550$ "upper branch" synchronized large amplitude $C_D(t_n)$ and $C_L(t_n)$ are restored.

The time-frequency analysis of the build-up shows the very low magnitude and quite effective phase of the synchronized force component in the intermediate region. A not synchronous vortex shedding shows larger amplitudes in the drag and lift time histories. At $t_n \ge 550$ transition to "upper branch" establishes large oscillation amplitudes $z^* > 1$, very large synchronous lift component $C_{L1} \approx 4.5$ and almost zero φ_{1Lz} phase.

Fig. 12. Build-up at $U_n = 1.28$ showing a clear transition from a stable state, intermediate between the "lower branch" and "upper branch" towards the "upper branch".

5. Reference time histories analysis: pressure distributions

The analysis of the instantaneous pressure distribution during the cylinder oscillation gave a clear understanding of the substantial transformation encountered by the pressure field on the cylinder during transition from the different states identified in the lock-in region. For each analysed build-up a set of four pressure distributions is plotted, corresponding, respectively, to: maximum velocity down (A), maximum displacement down (B), maximum velocity up (C) and maximum displacement up (D). This set has been plotted for different regions of the build-up time histories at different U_n. Referring to the $U_n = 1.17$ build-up given in Figs. 14–16, we see the pressure distributions encountered in the "first state" at cylinder oscillations $z^* < 0.2$, with asymmetric trends during situations of transient vortex shedding events (see Fig. 5 for integral quantities). At $t_n \simeq 105$ the transition is clearly marked by a transformation of the pressure distribution with an asymmetric trend strongly correlated to the cylinder oscillation. This gives a close view of the unsteady fluid-dynamic field governing the lock-in conditions (Fig. 17). At the end of the same build-up, with stable amplitudes $z^* \simeq 0.6$ and steady-state conditions, the large amplitude "upper branch" configuration is shown in Fig. 18.

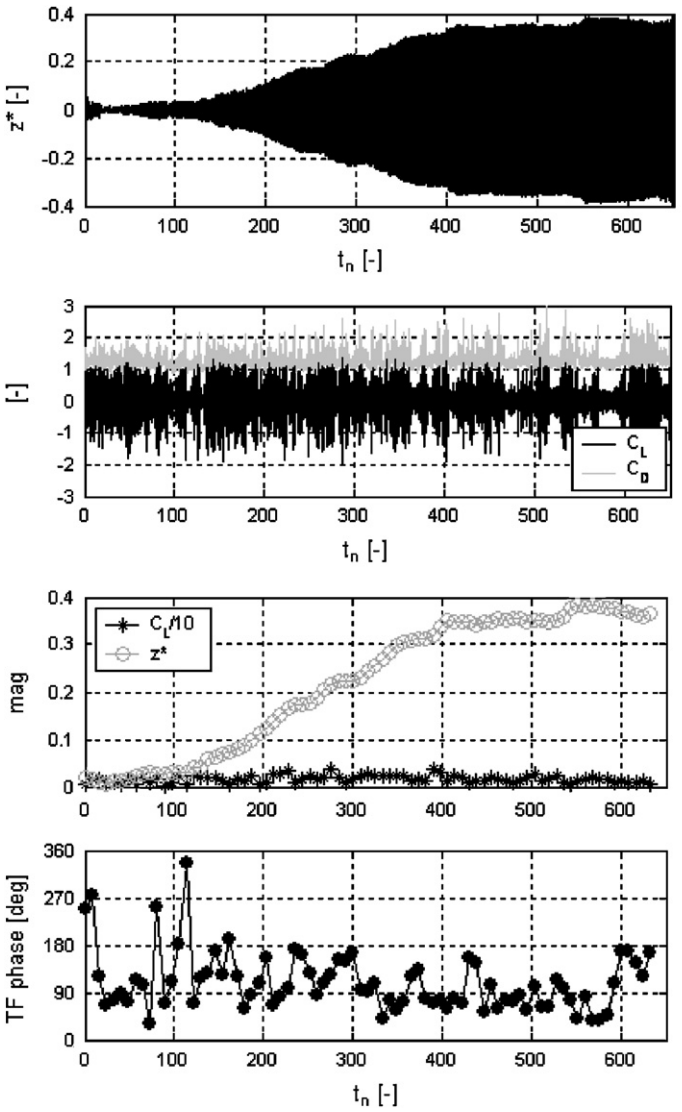

Build-up at U_n =1.3 close to the far right limit of the "lower branch" region. Quite large amplitudes z^* 0.4 are still measured showing irregular features both in build-up and in regime conditions.

Not synchronous vortex shedding is dominant in $C_D(t_n)$ and $C_L(t_n)$ time histories showing quite large peak lift values $C_L > 1$.

The time-frequency analysis of the build-up shows the low magnitude and quite effective phase of the synchronized force component in "lower branch". Making reference to the U_n =1.28 case it seems that the phase φ_{lLz} shows a tendency towards larger values increasing U_n. Intervals of 20-30 cycles with high phase values $(120° < \varphi_{lLz} < 180°)$ are present during build-up and at steady state

Fig. 13. Build-up at $U_n = 1.3$ showing the "lower branch" state at the exit from the synchronization field.

The stagnation point cannot be detected at anti-nodal (peak) conditions due to inertial effects. The stagnation point appears to rotate towards the relative wind velocity vector at zero cylinder deflection and maximum cross wind velocity. The integral lift on the section is clearly in phase with the displacement.

The build-up, reported in Fig. 19 (see Fig. 12 for integral quantities), documents the transition between an intermediate stable state at the borderline of the "lower branch" and the "upper branch". This build-up has been analysed at $t_n \simeq 617$ and $t_n \simeq 503$. Fig. 20(a), still referring to a transient condition, presents the final development of the pressure distribution at large $z^* \simeq 0.9$ in the "upper branch". Very large, asymmetric and perfectly oscillation-correlated pressure distributions generate the very strong oscillating lift characterized by $C_L > 4$. As already observed, large rotations of the relative wind velocity vector cause corresponding rotations of the stagnation point. On the other hand, due to prevailing inertial effects, the stagnation point disappears at anti-nodal (peak) conditions. Similar considerations also hold through Fig. 20(b) referring to the $z^* \simeq 1.25$ at $U_n = 1.25$ (see Fig. 4 for integral quantities). Due to the large cylinder velocities, the relative wind velocity vector shows rotations in the order of 45° resulting in relevant and surprising upwind suctions. At the same time, relevant inertial effects are shown, correlated to the cylinder large peak accelerations at maximum deflection, in the order of 100 m/s^2, resulting in a large $C_P > 0$ area with no clear evidence of stagnation point, rotated in agreement with the cylinder acceleration sign.

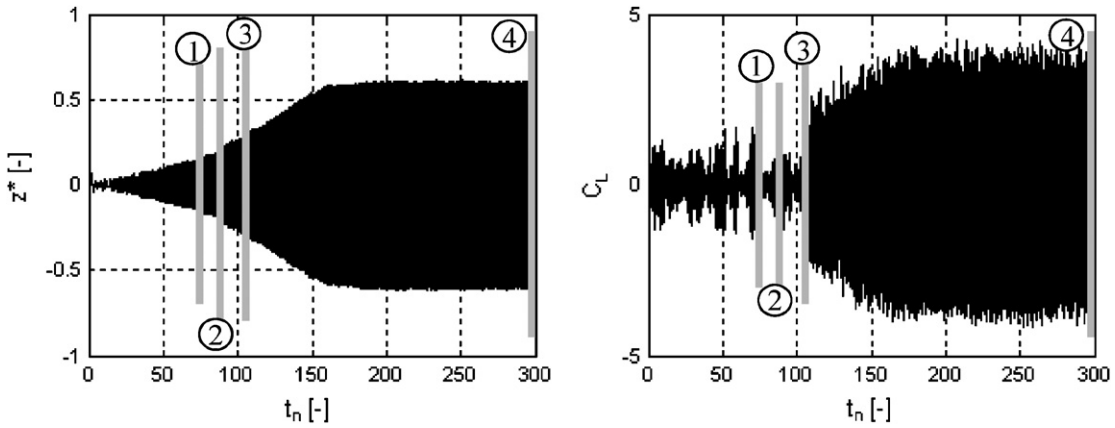

Fig. 14. Build-up at $U_n = 1.17$. The numbers on $z^*(t_n)$ and $C_L(t_n)$ time histories mark the position of the instantaneous pressure events analysed in the following plots.

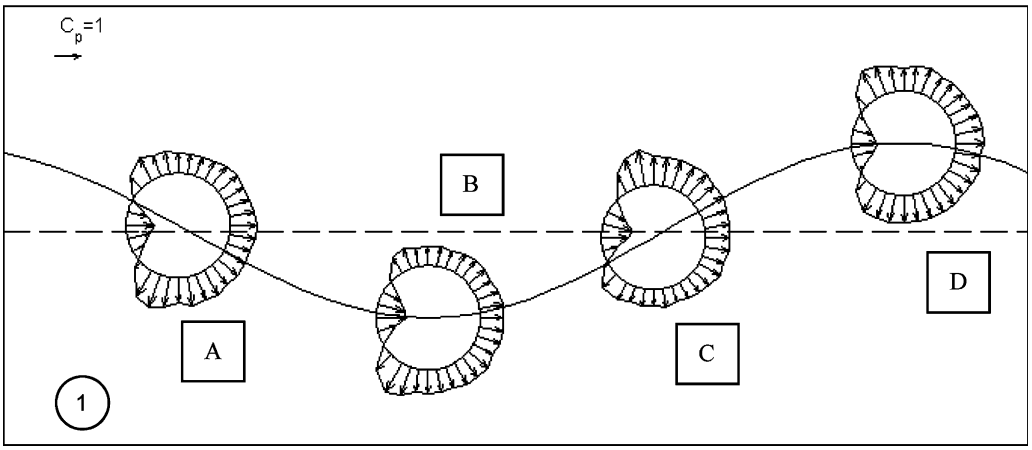

Fig. 15. $U_n = 1.17$, $t_n = 75$, $z^* = 0.17$. Pressure distribution $C_P(\vartheta; t_n)$ at "first state": no significant vortex shedding, no lock-in phenomena resulting in very symmetric C_P circumferential pressure distribution.

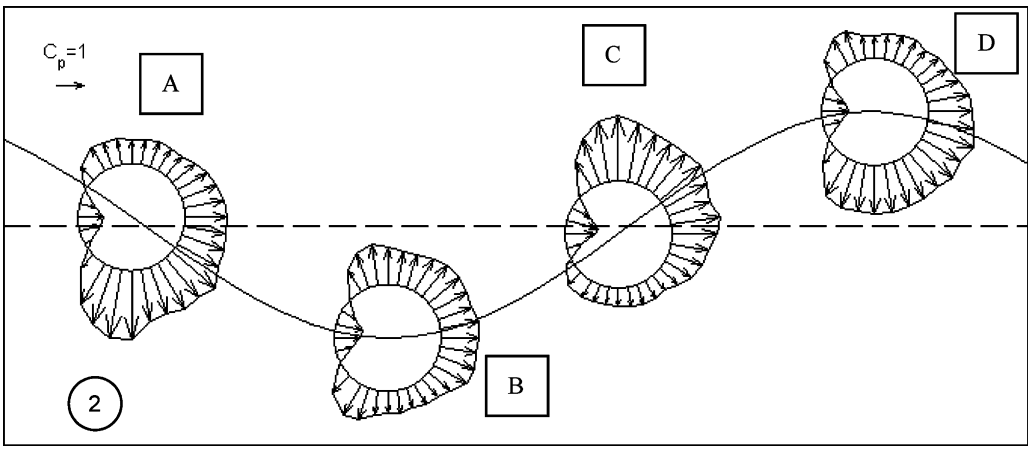

Fig. 16. $U_n = 1.17$, $t_n = 89$, $z^* = 0.2$. Pressure distribution $C_P(\vartheta; t_n)$ at "first state" during an event of unsynchronized vortex shedding, being $f_{vs} > f_s$. The C_P normalization is referred to the upstream undisturbed flow dynamic pressure $q_\infty = \frac{1}{2}\rho U_\infty^2$. The arrow at left corner gives the size of $C_P = 1$ for a quantitative reading.

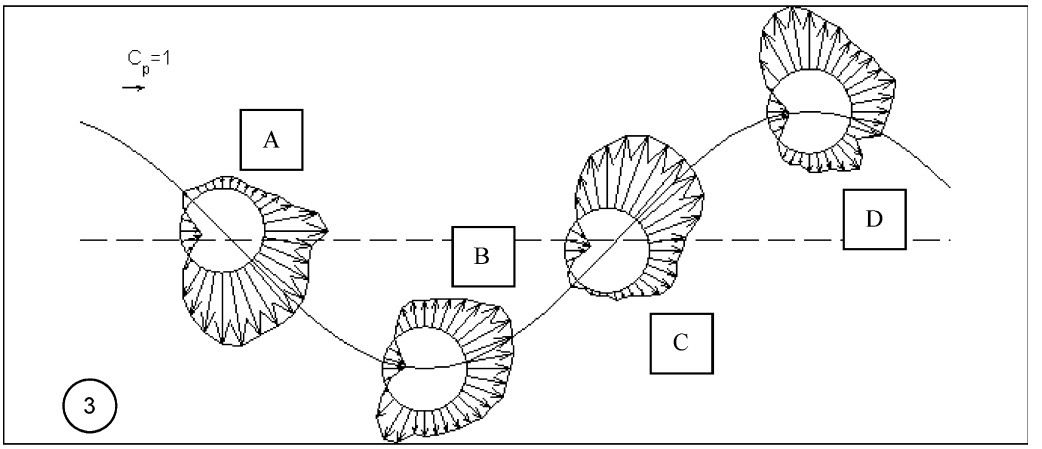

Fig. 17. $U_n = 1.17$, $t_n = 105$, $z^* = 0.3$. Pressure distribution $C_P(\vartheta; t_n)$ during transition: at quite small oscillation amplitudes a perfect correlation is found between pressure distribution and cylinder oscillation. Quite large C_P peak values are shown but still no significant effects on the stagnation point ($C_{P\mathrm{Max}} \simeq 4$).

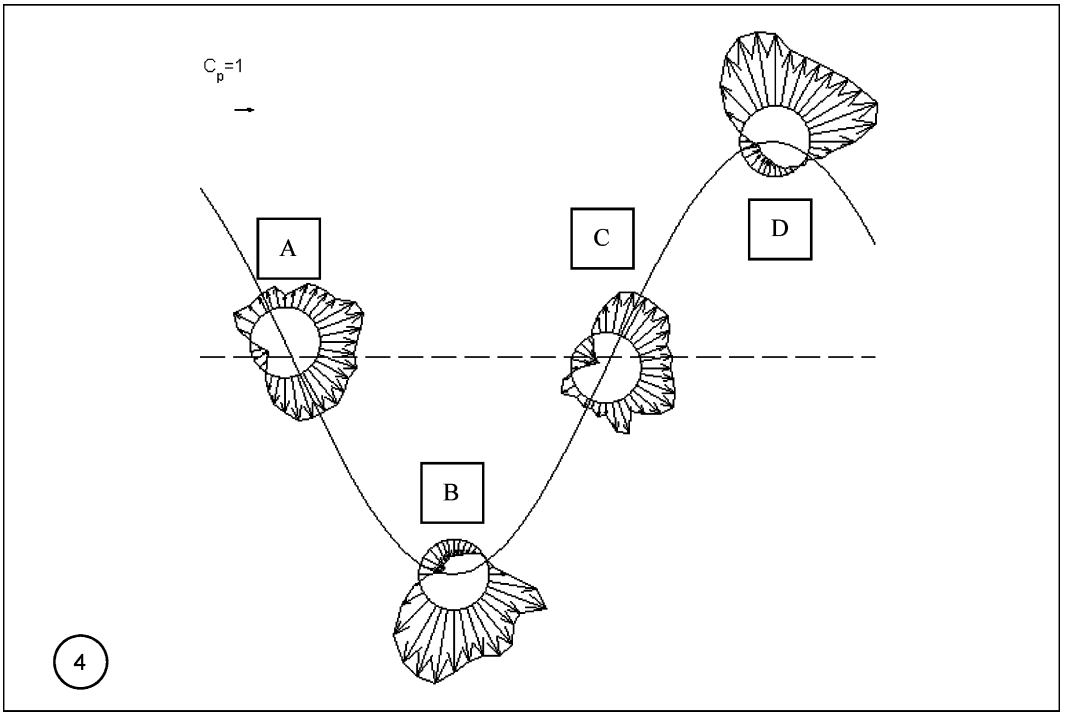

Fig. 18. $U_n = 1.17$, $t_n = 298$, $z^* = 0.6$. Pressure distribution $C_P(\vartheta; t_n)$ at stable steady-state amplitudes in the "upper branch" state: very large suctions are shown $C_{P\mathrm{Max}} > 4$ and peculiar $C_P > 0$ distributions at maximum deflection position, to be correlated with the very large cylinder peak accelerations $\ddot{z} = 50\ \mathrm{m/s^2}$. Very large oscillating lift $C_L \simeq 4$ values are reached as a result.

Fig. 21 shows the surprisingly very low C_P and very low asymmetric pressure distribution during the final stage of the steady-state intermediate regime just before transition (see Fig. 12 for integral quantities). It is worth noting that the cylinder oscillation amplitudes are quite large, i.e. $z^* \simeq 0.4$, larger than the values in Fig. 17 where oscillating lift $C_L \simeq 2$ was found. At such large amplitudes no vortex shedding occurred and the very low C_{L1} component shown in Fig. 12 was sufficient for sustaining the structural dissipations, thanks to the very effective $\varphi_{1Lz} \simeq 50^\circ$ phase. These large amplitudes cause a rotation of the stagnation point due to relative wind vector rotation. This regular pressure

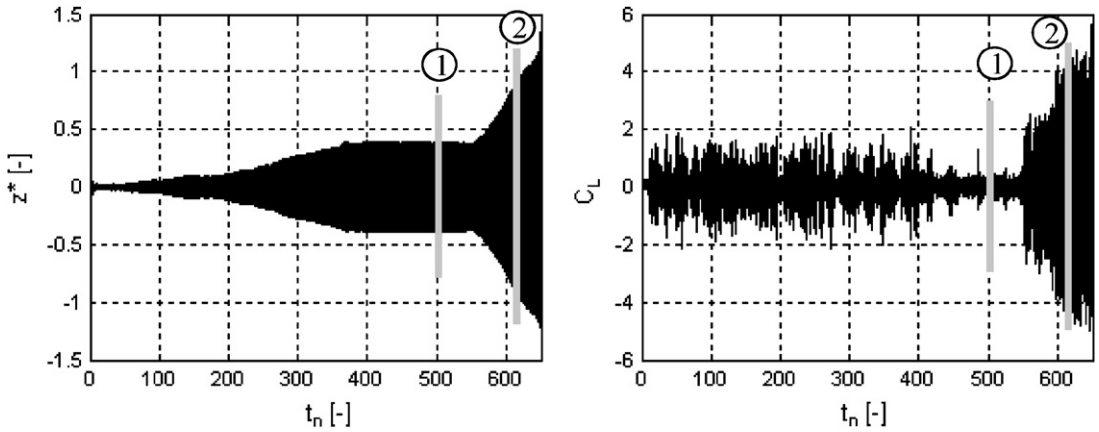

Fig. 19. Build-up at $U_n = 1.28$. Transition is shown from a stable state at the borderline of the "lower branch" to the "upper branch".

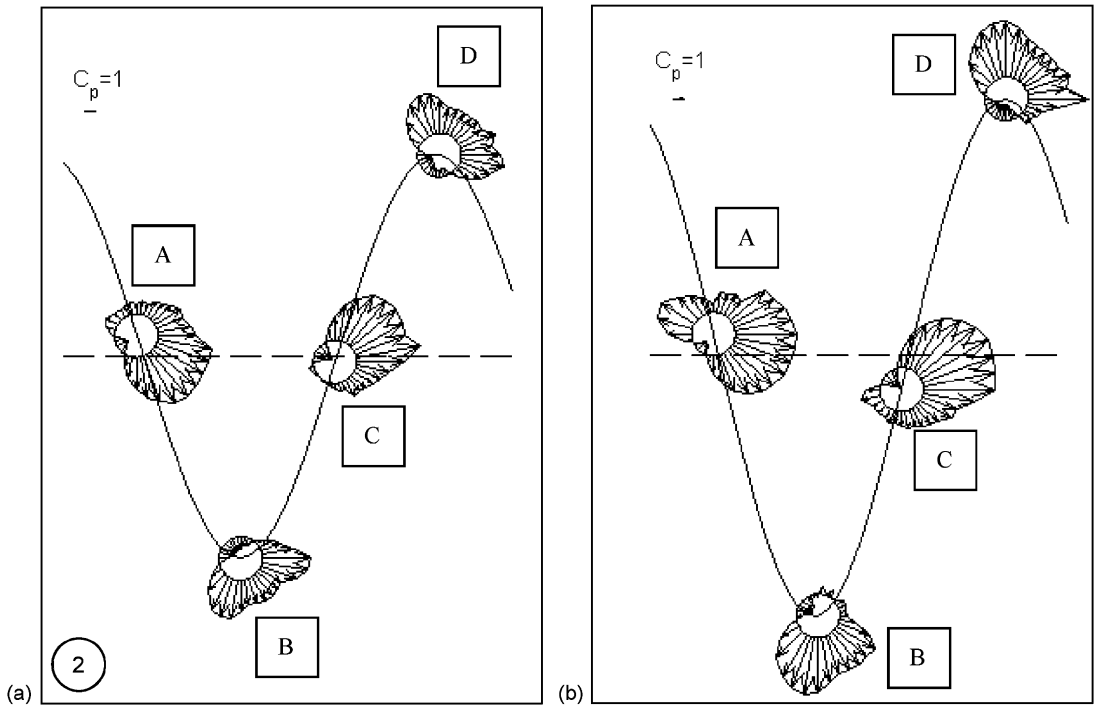

Fig. 20. Large amplitudes "upper branch" pressure distribution $C_P(\vartheta; t_n)$ at (a) $z^* = 0.9$(left) and (b) $z^* \simeq 1.2$ (right). At zero displacement crossing (A and C), i.e. max. cross-wind cylinder velocity there are very large suctions, $C_{P\mathrm{Max}} > 5$(left)–$C_{P\mathrm{Max}} > 6$ (right), and large stagnation point rotation resulting in upwind suctions (right). At max. deflection (B and D) large cylinder accelerations, $z^* = 0.9$, $\ddot{z} \simeq 75\ \mathrm{m/s^2}$(left) and $z^* \simeq 1.2$ $\ddot{z} \simeq 100\ \mathrm{m/s^2}$ (right), influence the pressure distributions in $C_P > 0$ region.

distribution is just the underlying configuration over which the unsynchronised Karman vortex shedding is superimposed, occurring at a frequency f_{vs} higher than the structural oscillation frequency f_s of the cylinder, with f_{vs}/f_s equal to $U_n = U_\infty / U_{vs}$. This situation is clearly shown in Fig. 22 in terms of pressure distribution and in Fig. 23 in terms of integral lift $C_L(t_n)$. These data have been obtained from the $U_n = 1.3$ build-up analysed in Fig. 13, representative of the "lower branch" state. Moreover, the nonstationary lift frequency is recognizable both in the force time history as well as in the instantaneous pressure distribution, being the vortex shedding frequency 30% higher than the one of the oscillating cylinder.

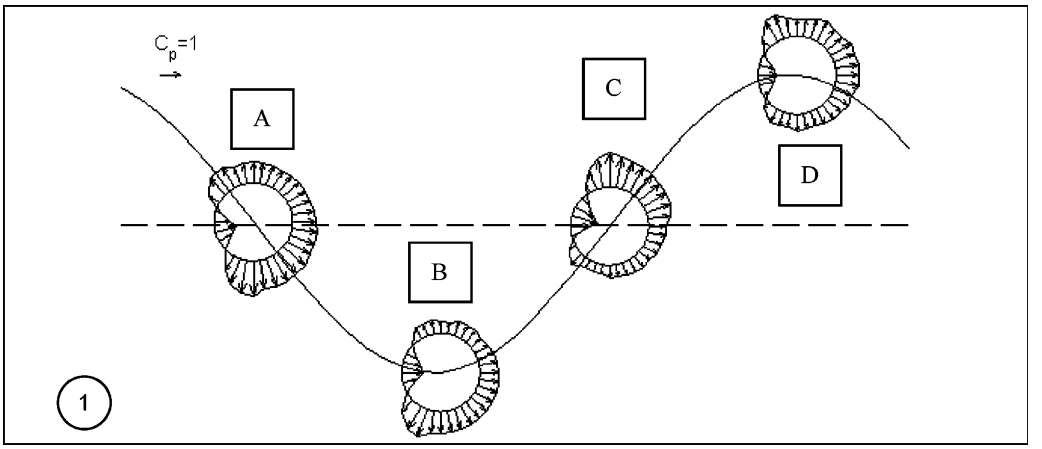

Fig. 21. $U_n = 1.28$, $t_n = 503$, $z^* = 0.4$. Pressure distribution $C_P(\vartheta; t_n)$ showing no vortex shedding, resulting in very symmetric C_P circumferential distribution.

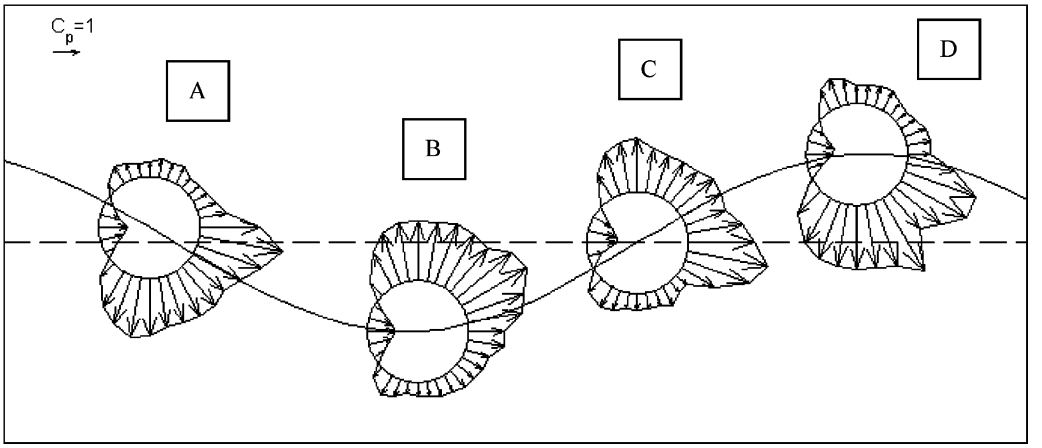

Fig. 22. $U_n = 1.3$, $t_n = 257$, $z^* = 0.17$. Pressure distribution $C_P(\vartheta; t_n)$ at "lower branch" during an event of non-synchronous vortex shedding: no lock-in phenomena resulting in very asymmetric, $C_P(\vartheta)$ circumferential distribution non-synchronous with the cylinder oscillations.

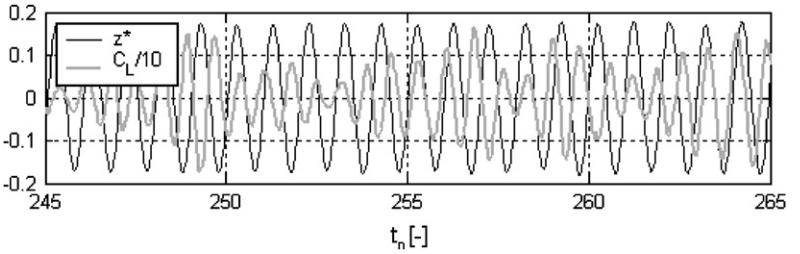

Fig. 23. $U_n = 1.3$: non-synchronous vortex shedding is evident in the "lower branch" state where the fundamental frequency of $C_L(t_n)$ is higher than the oscillation frequency of $z^*(t_n)$.

6. The special case $U_n = 1$

Special attention was given to the condition $U_n = 1$ at which $f_{vs} \equiv f_s$ was expected, being $U_\infty = U_{vs}$, or in other words where Karman vortex shedding was expected to be perfectly synchronized with the cylinder natural frequency. In fact, all the analysis showed vortex shedding perfectly synchronous with the cylinder oscillation, with quite large $C_{L1} \simeq 1$

amplitude but surprisingly resulting in very low $z^* \simeq 0.1$ cylinder oscillations. The time-frequency analysis described above on the integral quantities and the consequent evaluation of the power input associated with the flow–cylinder interaction allowed us to clearly justify the absence of dynamic amplification, despite the cylinder being excited by a vortex shedding force apparently "in resonance".

Fig. 24 shows the usual quantities $z^*(t_n)$, $C_D(t_n)$, $C_L(t_n)$, $C_{L1}(t_n)$, $z_1^*(t_n)$, $\varphi_{1Lz}(t_n)$ and the normalized power input $\overline{W}_{\mathrm{Norm}}$ as functions of the nondimensional time t_n. The amplitudes are always limited to $|z^*(t_n)| < 0.1$, when the

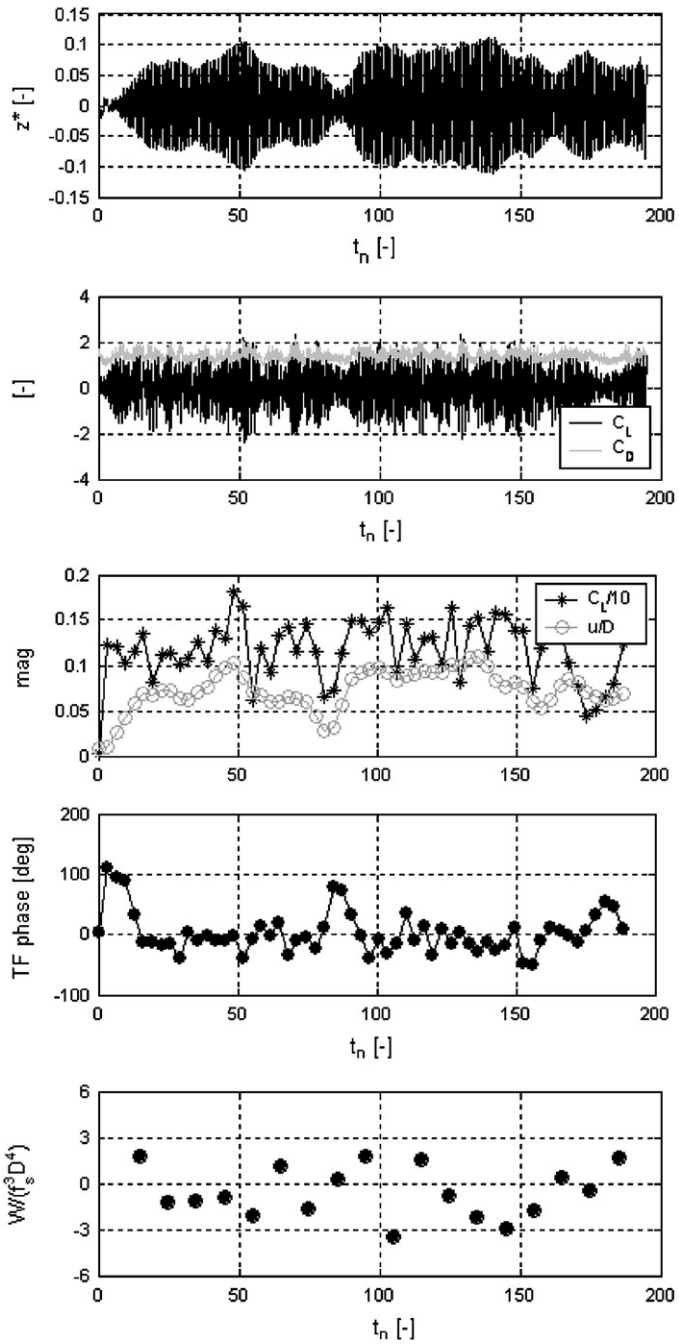

Limited amplitude oscillations observed at $U_n = 1$. The vibration amplitude does not reach a stable limit value, but shows a continuous alternation of expansive and damped build-up reaching maximum level $z^* \approx 0.1$.

$C_D(t_n)$ and $C_L(t_n)$ plots show vortex shedding perfectly synchronized with the displacement $z^*(t_n)$ resulting in quite large dynamic lift amplitude $|C_L(t_n)| \approx 2$. Not stable amplitudes but a continuous alternation of about 10 cycles "burst" is the typical feature encountered.

The time-frequency analysis of the transient oscillations shows quite large levels of synchronized force component $1 < C_{L1}(t_n) < 1.5$ evaluated by averaging on a 10 cycles moving window. The phase $\varphi_{1Lz}(t_n)$ is oscillating around zero showing some short and well defined intervals of $\varphi_{1Lz} \approx 90°$ correlated with $z^* \approx 0$ amplitudes. Strong correlation is finally shown between growing oscillation amplitudes and decreasing phase.

The oscillation around zero is well justified by the phase trend discussed above. Although being available a relevant force perfectly synchronized with the oscillation no power input is allowed.

Fig. 24. Build-up at $U_n = 1.0$. Time histories and time-frequency analysis.

instantaneous dynamic lift is not negligible, reaching values in the order of $|C_L(t_n)| \simeq 2$. The time frequency analysis shows that the synchronous lift component $C_{L1}(t_n)$ is always in the order of $1 < C_{L1}(t_n) < 1.5$, and finally the relative phase shows a clear tendency of being $\varphi_{1Lz}(t_n) \leqslant 0$. More precisely, at very low amplitudes, phases $\varphi_{1Lz}(t_n) \gg 0$ (close to 90°) are shown, and as a consequence $z^*(t_n)$ amplitudes grow. On the other hand, as the amplitudes grow, the phase is pushed towards negative values, damping the cylinder oscillations and limiting them to quite small levels. The integration of the instantaneous power input over the moving windowed 10 cycles finally shows very limited values and a continuous oscillation over the zero line, in agreement with the phase indications. In other words there is no possibility of positive power input despite the vortex shedding being at the same frequency as the oscillating cylinder. The reason for this is that the flow–structure interaction drives the phase of the lift force to values ineffective in terms of power input into the mechanical system. A very clear understanding of the mechanism controlling the limited cylinder oscillations is given by the zoomed observation of $z^*(t_n)$ and $C_L(t_n)$ time histories shown in Fig. 25. At $z^* \simeq 0$ in the interval $0 < t_n < 15$ the lift force has a positive phase allowing evident growth of the oscillation amplitudes but, when the amplitudes approach $z^* \simeq 0.1$, the phase is pushed to zero or even to negative values. The link described above between the oscillation amplitudes z^* and the relative phase φ_{1Lz} of the lift force acts as feedback and limits the oscillations to small values. This is shown in the interval $70 < t_n < 100$. The force and the oscillation are in fact perfectly synchronized, but the phase moves slightly, from negative values, associated to the highest z^* level, to zero and then to positive values as a consequence of the very small z^*, starting the cycle again.

The peculiar situation where $U_n = 1$ clearly showed a vortex shedding frequency equal to the natural oscillation frequency of the cylinder with non-negligible C_{L1} values but with a deterministic and systematic phase tendency towards negative values at growing amplitudes. As a consequence no power input is allowed resulting in $z^* \simeq 0$ at $U_n = 1$, and confirming the well-documented experience of response curves in z^* versus U_n plane shifted in the region $U_n > 1$. It was confirmed that the phase φ_{1Lz} is a function of $\{z^*, U_n\}$ showing a very strong negative z^* gradient at $U_n = 1$, starting from very effective $\varphi_{1Lz} \simeq 90°$ at $z^* \simeq 0$ and sinking rapidly to zero and below-zero values as soon as z^* grows over $z^* \geqslant 0.05$. The main finding of this analysis, at $U_n = 1$, is the existence of direct feedback between oscillation amplitude and relative phase force displacement. As far as is known by the authors, this has not been well described in literature yet.

7. Main findings: synthesis and interpretation

The experimental research allowed the detection and description of some important mechanisms governing the vortex shedding excitation of a circular cylinder in a narrow field around $\mathrm{Re} \simeq 5 \times 10^4$ in the lock-in region. Three fundamental states have been encountered at the expected location in the z^* versus U_n plane, two of them clearly corresponding to the well-known "upper branch" and "lower branch" states, fully described in literature. What has been called "first state", in the authors' opinion, does not correspond with the "initial state" described in literature for the initial branch (low U_n) of the response curve. In fact, the "first state" is positioned at much lower amplitudes z^* in the area underneath the progressive regimes response curve in the z^* versus U_n plane. This state is characterized by phase values $\varphi_{1Lz} \simeq 90°$, which could be compared with the corresponding phase values $\varphi_{1Lz} \simeq 0°$ quoted in the literature for the "initial state", and confirmed by the present measures as shown in Fig. 10.

The low damping ξ_s of the mechanical system realized in the experimental set-up, results in low mass-damping $m^*\xi_s$ (or equivalent Scruton number Sc*), which allowed us to reach large amplitudes z^* and to identify the transition between different states. In particular, a relationship governing the transition between the "first state" and the "upper branch" state was experimentally observed, as shown in Fig. 6, proving that the transition occurs at the condition of $z^* > z^*_{\mathrm{threshold}}(U_n)$ with larger z^* at higher U_n.

Considering the well-defined limits in the maximum power input (Diana and Falco, 1971; Brika and Laneville, 1993; Diana et al., 2005a, b), taking into account the relation (7) and the mass-damping parameter Sc*, a consequence of the identified threshold level is that a limiting value Sc* can be defined over which no "upper branch" state can exist regardless of U_n. Where no "upper branch" can exist, the cylinder response with increasing U_n shows a direct transition from the "initial state" to the "lower branch" state. The transition is explained in terms of integral quantities plotting families of coefficients $C_{L1}(z^*, U_n)$ and $\varphi_{1Lz}(z^*, U_n)$ as functions of z^* assuming U_n as a parameter (see Figs. 26(a) and (b)). Low values C_{L1} and close to 90° phases φ_{1Lz} are shown at the "first state", until the amplitudes reach a threshold level $z^*_{\mathrm{threshold}}(U_n)$, function of U_n. After this level the "upper branch" is reached and it is characterized by large vibration amplitudes, close to zero positive phases and large synchronized lift values. The plotted trends come from transient build-up tests but they can be representative of quasi-stationary oscillation amplitudes because the mechanical transient typical time τ_M is very large compared to the fluid-dynamic characteristic time τ_A. In quantitative

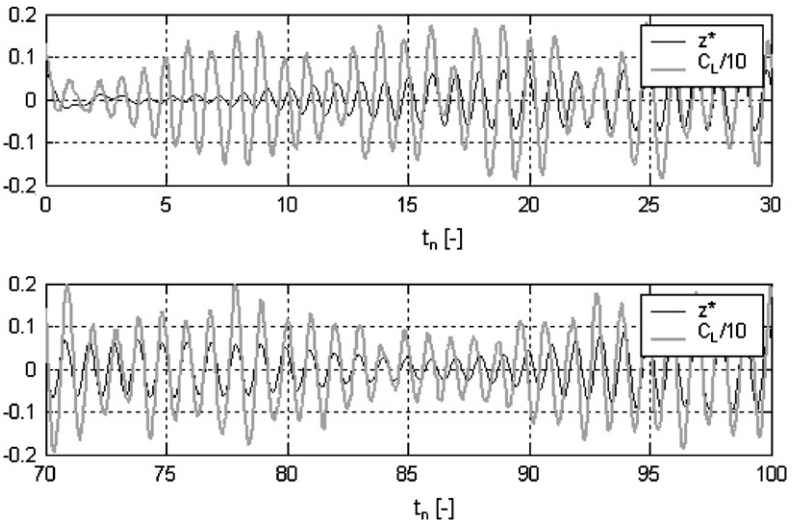

Fig. 25. Examples of build-up at $U_n = 1.0$ showing perfectly synchronized vortex shedding with self-limiting cylinder oscillations through a clear feedback from amplitudes z^* and phase $\varphi_{1Lz}(z^*)$.

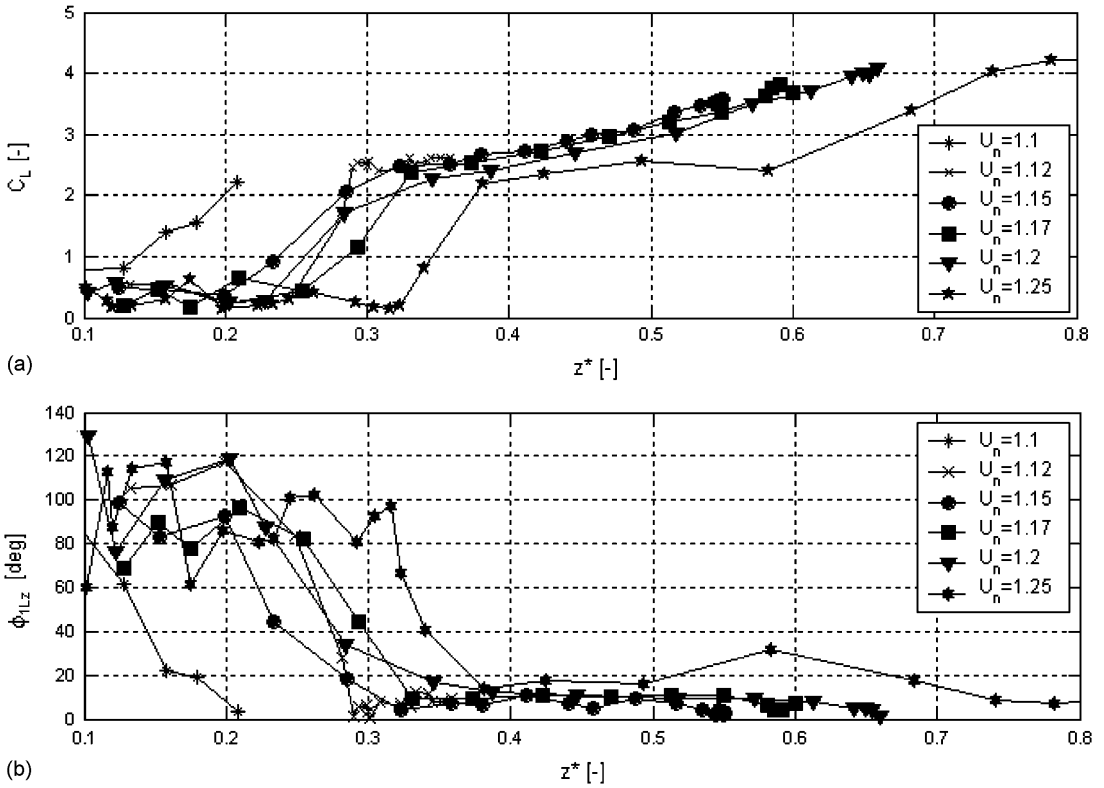

Fig. 26. (a) $C_{L1}(z^*;U_n)$ trend as a function of z^*; (b) $\varphi_{1Lz}(z^*;U_n)$ trend as a function of z^*.

terms the mechanical characteristic transient time τ_M is associated with the exponential trend oscillations e^{t/τ_M} resulting in $\omega_s\xi_T = 1/\tau_M$, ξ_T being the already defined build-up exponential trend.

The fluid-dynamic characteristic time can be defined as $\tau_A = D/U_\infty$, so that the ratio τ_M/τ_A can be written as follows: $\tau_M/\tau_A = (V^*/2\pi)(1/\xi_T)$. For the considered case $(V^*/2\pi)$ is nearly equal to 1 and so the time ratio can be

written as $\tau_M/\tau_A \simeq 1/\xi_T$. The fastest build-up observed from the present research is characterized by $\xi_T \simeq 5 \times 10^{-3}$. This confirms the hypothesis that the fluid-dynamic interaction is faster than the mechanical system dynamics. So it becomes possible to extent the given relationships $C_{L1}(z^*;U_n)$, $\varphi_{1Lz}(z^*;U_n)$ more generally than the specific build-up in which they have been measured. A deeper analysis concerning this assumption is the object of ongoing research.

8. Conclusion

The experimental set-up, focused on the measurement of unsteady pressure distribution on the oscillating cylinder surface, allowed a quantitative understanding of the flow–cylinder interaction and of the vortex shedding features. Special attention has been devoted to a detailed enquiry about the phase relationship between the interaction force on the cylinder and the cylinder displacement. It was clear that a time domain approach was not adequate to understand the core of the forcing mechanism sustaining the cylinder vibration in the wide lock-in region. A frequency domain approach was needed to clarify the role of the force component at the same frequency of the oscillation. This component is, in fact, the only one responsible for supplying power to the cylinder motion, and it is always present also during non-synchronous vortex shedding events. Three different fluid-dynamic states have been described, both in terms of unsteady pressure distribution as well as in terms of integral quantities the ''first state'', ''upper branch'' and ''lower branch''. The ''initial state'' described in the literature, being very similar to the ''upper branch'' in terms of phase φ_{1Lz}, was not specifically distinguished in the analysed data, even if it was documented in the initial portion (at low U_n) of the response curve. Vortex shedding synchronous with the oscillating cylinder frequency was documented at $U_n = 1$, but surprisingly with very limited cylinder oscillations. This is due to the direct feedback between amplitude and phase, pushing the phase to negative values when the oscillation amplitudes reach $z^* \simeq 0.1$ values. The vortex shedding was found to be non-synchronous at $U_n \neq 1$ and low z^* unless the transition to ''initial state'' or to ''upper branch'' state occurs. The amplitudes needed for transition increase as a function of increasing U_n. Except for when $U_n = 1$, the condition in which the vortex shedding is of perfectly equal frequency with the cylinder oscillation is defined as ''lock-in''. The lock-in region should be limited to the post-transition region, when the ''initial branch'' or the ''upper branch'' states have been reached. The ''first state'' and the ''lower branch'' show a vortex shedding non-synchronized with the cylinder oscillation, but there is a positive power input due to the presence of a small but very phase-effective equal frequency component. This allows a wider response curve to the far right limit outside of the proper ''lock-in'' region with ''lower branch'' fluid-dynamic state. A first attempt of experimental description of the constitutive law linking the magnitude and the phase of the isofrequent interaction force component with the fluid-dynamic state $\{U_n, z^*\}$ gives rise to the well-defined and quite regular plots including the quantitative description of the transition phenomenon (Figs. 26(a) and (b)).

The ongoing research is now focused on the correlation analysis between the pressures measured on different cylinder sections (Zasso et al., 2006) and on a possible comparison between the measured unsteady pressure data and the numerical simulation results. The purpose is to correlate the peculiar pressure distributions encountered, and their transformation, with the topology of the flow and vortex structures interacting with the oscillating cylinder.

References

Brika, D., Laneville, A., 1993. Vortex induced vibrations of a long flexible circular cylinder. Journal of Fluid Mechanics 250, 481–508.

Carberry, J., Sheridan, J., 2001. Forces and wake modes of an oscillating cylinder. Journal of Fluids and Structures 15, 523–532.

Carberry, J., Govardhan, R., Sheridan, J., Rockwell, D., Williamson, C.H.K., 2004. Wake states and response branches of forced and freely oscillating cylinders. European Journal of Mechanics B 23, 89–97.

Chen, S., 1993. Flow-induced Vibration of Circular Cylindrical Structure. Springer, Berlin.

Diana, G., Falco, M., 1971. On the forces transmitted to a vibrating cylinder by a blowing fluid. Meccanica International Journal 6 (1), 9–22.

Diana G., et al., 2005a. Progetto Speciale di Ateneo: Interazione Fluido Struttura. Report 2004–2005, Politecnico di Milano, Italy.

Diana, G., Belloli, M., Resta, F., Muggiasca, S., 2005b. Experimental analysis on vortex induced vibration of a long flexible cylinder. In: Proceedings of the 6th International Symposium on Cable Dynamics, Charleston SC, USA.

Diana, G., Zasso, A., Vigevano, L., Auteri, F., Formaggia, L., Nobile, F., 2006. Flow–structure interaction of the oscillating cylinder in the lock-in region: computational versus experimental approach comparison. In: Proceedings of the 4th International Symposium on Computational Wind Engineering, Yokohama, Japan.

Feng, C.C., 1968. The measurements of vortex-induced effects in flow past a stationary and oscillating circular and D sections cylinders. Master's Thesis, University of British Columbia, Vancouver, BC, Canada.

Govardhan, C., Williamson, C.H.K., 2000. Modes of vortex formation and frequency response of a freely vibrating cylinder. Journal of Fluid Mechanics 420, 85–130.

Khalak, A., Williamson, C.H.K., 1999. Motions, forces and mode transitions in vortex-induced vibrations at low mass-damping. Journal of Fluids and Structures 13, 813–851.

Sarpkaya, T., 2004. A critical review of the intrinsic nature of vortex-induced vibrations. Journal of Fluids and Structures 19, 389–447.

Simiu, E., Scanlan, H., 1996. Wind Effects on Structures. Wiley, New York.

Willden, R.H.J., 2006. Numerical simulation of the multiple branch transverse response of a low mass ratio elastically supported circular cylinder. In: Proceedings of the FSI, AE&FIV + N Symposium, ASME PVP2006-ICPVT-11, Vancouver, BC, Canada.

Williamson, C.H.K., Roshko, A., 1988. Vortex formation in the wake of an oscillating cylinder. Journal of Fluids and Structures 2, 355–381.

Zasso, A., Manenti, A., Belloli, M., Giappino, S., Muggiasca, S., 2005. Energy input by the flow on a vibrating smooth circular cylinder in cross flow at $\mathrm{Re} = 5 \times 10^4$. In: Proceedings of the 6th International Symposium on Cable Dynamics, Charleston SC, USA.

Zasso, A., Belloli, M., Giappino, S., Muggiasca, S., 2006. On the pressure and force field on a circular cylinder oscillating in the lock-in region at sub-critical Reynolds number. In: Proceedings of the ASME PVP2006-ICPVT-11, Vancouver, BC, Canada.